Isogeometric shape optimization on triangulations[*]

Cunfu Wang Songtao Xia Xilu Wang Xiaoping Qian[†]

Department of Mechanical Engineering
University of Wisconsin-Madison
1513 University Avenue, Madison, WI 53706

Abstract

The paper presents a Bézier triangle based isogeometric shape optimization method. Bézier triangles are used to represent both the geometry and physical fields. For a given physical domain defined by B-spline boundary, a coarse Bézier triangular parameterization is automatically generated. This coarse mesh is used to maintain parameterization quality and move mesh by solving a pseudo linear elasticity problem. Then a fine mesh for isogeometric analysis is generated from the coarse mesh through degree elevation and refinement. As the fine mesh retains the same geometric map as the coarse mesh, we can guarantee mesh validity with the coarse mesh only. This bi-level mesh allows us to achieve high numerical accuracy of isogeometric analysis and lower computational cost on mesh validity control and mesh movement. Due to the use of B-spline boundary, the optimized shape can be compactly represented with a relatively small number of optimization variables. Due to the use Bézier triangles, this shape optimization method is applicable to structures of complex topology and allows for local refinement for analysis. By representing the squared distance between two Bézier curves as a Bézier form, a distance check scheme is also introduced to prevent intersections of design boundaries and control the thickness of structural connections. Numerical examples on minimal compliance design and design of negative Poisson ratios are presented to demonstrate the efficacy of the proposed method.

Keywords Isogeometric analysis, Bézier triangles, Jacobian ordinates, Distance constraints, Coarse and fine mesh, Material design, Negative Poisson's ratio

1 Introduction

Shape optimization is a classic discipline that seeks to find optimal shape to improve structural performances under certain physical constraints [1, 2, 3]. Both moving mesh [4, 5] and fixed grid based shape optimization methods [6, 7] have been proposed. The goal of this paper is to present a Bézier triangle based isogeometric shape optimization method.

[*] An earlier version of this paper appeared in 2016 ASME International Design Engineering Technical Conferences.

[†] Corresponding author. Email: qian@engr.wisc.edu

Isogeometric analysis (IGA) is a numerical method for solving partial differential equations (PDEs) in which same basis functions are used both to represent the geometric models and to approximate the state fields. It enjoys many numerical advantages, such as computational efficiency on a per-node basis, over traditional finite element analysis[8]. Due to the same geometry being used in design and analysis, it thus alleviates the usual burden of model conversion, approximation and discretization in preparing the analysis model from the design geometry. Isogeometric shape optimization [9, 10, 11] is a shape optimization method where the same basis are also used to parameterize the shape, in addition to being used for analysis. It thus inherits the advantages of isogeometric analysis and the resulting shape can be directly imported into CAD systems, leading to closer integration of design and analysis.

Non-uniform rational B-spline (NURBS) is the de facto standard representation of geometries in CAD systems. It has been widely used in IGA [8] and in isogeometric shape optimization. Usually, the coordinates of NURBS control points are selected as optimization variables [9, 10]. The weights of NURBS control points are first considered as design variables in [11]. An approach of shape optimization based on the isogeometric boundary element is also proposed in [12]. The semi-analytical sensitivity analysis and sensitivity weighting techniques are proposed recently in [13] to avoid the effects of the chosen discretization on the design update. In [14], the discretization-dependency of the shape gradient is investigated and normalization approaches are proposed to obtain a discretization-independent normalized descent search direction. In the last few years, the applications of isogeometric shape optimization have expanded from elasticity to vibrating membranes[15], photonic crystals [16], electromagnetic scatterers [17] and fluid mechanics [18]. Isogeometric shape optimization has also been successfully integrated with sizing optimization [19] and material distribution optimization [20, 21].

Due to the tensor-product nature of NURBS surfaces, NURBS-based isogeometric shape optimization only works well for quadrilateral design domains. A number of methods have been proposed to overcome the limitation. A natural solution is to subdivide the design domain of complex topology into multiple quadrilateral patches. Qian and Sigmund [16] used a collection of Coons patches to represent the topologically complex geometries. The interior control points are determined for each Coons patch and their nodal sensitivities with respect to the boundary control points are analytically calculated. Similarly, Manh et al [15] utilized multiple quadrilateral patches to represent the vibrating membranes whose shapes could be allowed to change freely. Another way to handle the limitation of tensor product characteristic is using trimmed surfaces [22]. Although these methods can handle the complex topology issue to some extent, how to automatically construct NURBS parameterization of a given design domain of complex topology remains a challenging research issue.

In this paper, we present a new isogeometric shape optimization method that is applicable to topologically complex design domain. This approach is based on isogeometric analysis on Bézier triangulations [23, 24, 25] where the design domain and physical fields are represented through Bézier triangles. With this approach, for a given arbitrary design domain defined with B-splines boundary, a coarse Bézier triangular parameterization is automatically generated following the procedure presented in [23, 24]. This coarse mesh is then used to evaluate mesh quality and to solve a pseudo linear elasticity problem for mesh movement during shape optimization. A fine mesh for conducting isogeometric analysis is then constructed from the coarse mesh through refinement and/or degree elevation. The resulting fine mesh retains the same geometric map as the coarse mesh. Such a consistent bi-level mesh makes it possible to avoid mesh self-intersection and to guarantee mesh validity during shape optimization with constraints on the Jacobian ordinates of the coarse mesh only. In this way, the number of Jacobian ordinates (or constraints) is relatively small. This bi-level mesh also allows the use of fine Bézier triangles based analysis for numerical accuracy.

To prevent intersections of different design boundaries and control the minimum thickness of connections, a distance check scheme is also introduced. This is implemented by representing the squared distance between two Bézier curves as a Bézier form and imposing constraints on the resulting Bézier ordinates.

In this paper, the proposed isogeometric shape optimization method has been extended to classical minimal compliance design problem as well as the design of materials with negative Poisson's ratio (NPR). Such materials(also called auxetic materials) shrink/expand laterally when compressed/stretched axially. A comprehensive review of auxetic materials can be found in [26]. Although topology optimization has been routinely used to design auxetic materials [27, 28, 29], shape optimization is seldomly used to design auxetic materials. Finite-element based shape optimization is employed in [30] to guarantee uniform member sizes. Recently, NURBS-based isogeometric shape optimization is applied to design star-shaped auxetic materials [31]. Compared with NURBS representation in [31], Bézier triangles allow us to design unit cells with complex topology. Furthermore, as the unit cells of the auxetic cellular structures tend to thin connections, the proposed bi-level meshes become especially advantageous. The coarse mesh is used to maintain mesh validity and move mesh. The fine mesh is only used to conduct analysis. The optimized unit cells are periodically repeated to generate cellular structures. These cellular structures are represented by B-spline boundaries and parameterized by Bézier triangles. The B-spline representation allows us to link directly the optimized design to CAD systems and the Bézier triangular mesh allows us to conduct analysis and verify the NPR behavior.

We detail our approach below after a brief review of the basics of B-splines and Bézier triangles in Section 2. Section 3 describes the procedures to automatically generate Bézier triangular mesh for a given design domain defined by B-splines boundary. The Jacobian ordinates of Bézier triangles are derived in Section 4. These ordinates are used in the optimization to guarantee mesh validity. Section 5 formulates the optimization problem and illustrates the Bézier triangle based isogeometric shape optimization method. Formulations for auxetic materials design are also described. The shape sensitivities of the objective function and constraints are derived in Section 6. Section 7 provides numerical examples to demonstrate the proposed method. Finally, conclusions are drawn in Section 8.

2 B-splines and Bézier triangles

In the present work, we use B-splines to represent the domain boundary and Bézier triangles to parameterize the design domain and conduct isogeometric analysis.

2.1 B-splines

A B-spline curve of degree d and $n+1$ control points is defined as [32]

$$\mathbf{C}(u)=\sum_{i=0}^{n}\mathbf{c}_iR_{i,d}(u), \tag{1}$$

where $\mathbf{c}_i$ is the i-th control point, and $R_{i,d}$ is the i-th B-spline basis function for a given parameter u.

2.2 Bézier Triangles

A single span of a B-spline curve is a Bézier curve which can be defined by Bernstein polynomials. The $d+1$ Bernstein polynomials of degree d read

$$B_{\mathbf{i},d}(\xi)=\frac{d!}{i!j!}\xi^i(1-\xi)^j, \quad |\,\mathbf{i}\,|=i+j=d. \tag{2}$$

Accordingly, a Bézier patch can also be defined by bivariate Berstein polynomials. The d-th degree bivariate Berstein polynomial can be defined as

$$B_{\mathbf{i},d}(\boldsymbol{\xi})=\frac{d!}{i!j!k!}\xi_1^i\xi_2^j\xi_3^k, \quad |\,\mathbf{i}\,|=i+j+k=d, \tag{3}$$

where $\mathbf{i}$ represents a triple index (i,j,k). Let $\mathbf{v}_1,\mathbf{v}_2,\mathbf{v}_3$ be the vertices of a triangle τ and $(s,t)\in\mathbb{R}^2$ be a point in τ, then $\boldsymbol{\xi}\equiv(\xi_1,\xi_2,\xi_3)$ is the barycentric coordinate of the point (s,t), i.e.

$$(s,t)=\xi_1\mathbf{v}_1+\xi_2\mathbf{v}_2+\xi_3\mathbf{v}_3, \quad \xi_1+\xi_2+\xi_3=1. \tag{4}$$

A triangular Bézier patch is defined as

$$\mathbf{x}(\boldsymbol{\xi})=\sum_{|\mathbf{i}|=d}\mathbf{p}_{\mathbf{i}}B_{\mathbf{i},d}(\boldsymbol{\xi}), \tag{5}$$

where $\mathbf{p}_{\mathbf{i}}$ represent control points of the patch. The number of control points is $n_c=\frac{(d+1)(d+2)}{2}$. In the context of isogeometric analysis, Eq. (5) can be rewritten as

$$\mathbf{x}(\boldsymbol{\xi})=\mathbf{N}^{\mathsf{T}}\mathbf{p}=\sum_{l=1}^{nc}N_l\mathbf{p}_l, \tag{6}$$

where $\mathbf{N}$ represents the shape function matrix. Hence, each isogeometric element has n_c control points.

For isogeometric analysis, the same bivariate Bernstein polynomials defining a triangle $\tau=\{\mathbf{v}_1,\mathbf{v}_2,\mathbf{v}_3\}$ can be used to define a polynomial function $f(\boldsymbol{\xi})$ of degree d over τ as

$$f(\boldsymbol{\xi})=\sum_{|\mathbf{i}|=d}b_{\mathbf{i}}B_{\mathbf{i},d}(\boldsymbol{\xi}), \tag{7}$$

where $b_{\mathbf{i}}$ (or b_{ijk}) are Bézier ordinates of $f(\boldsymbol{\xi})$. Their associated domain points $\mathbf{q}_{i,j,k}$ in the triangle τ are defined as

$$\mathbf{q}_{ijk}=\frac{i\mathbf{v}_1+j\mathbf{v}_2+k\mathbf{v}_3}{d},\ i+j+k=d. \tag{8}$$

Then $(\mathbf{q}_{ijk}, b_{ijk})$ denote the control points of the polynomial function $f(\boldsymbol{\xi})$. The function $f(\boldsymbol{\xi})$ can be evaluated over the triangle τ through the de Casteljau algorithm [33]. $f(\boldsymbol{\xi})$ is equal to $b^d_{(0,0,0)}(\boldsymbol{\xi})$ and $b^r_{\mathbf{i}}(\boldsymbol{\xi})$ is calculated as

$$b^r_{\mathbf{i}}(\boldsymbol{\xi}) = \xi_1 b^{r-1}_{\mathbf{i}+\mathbf{e}_1}(\boldsymbol{\xi}) + \xi_2 b^{r-1}_{\mathbf{i}+\mathbf{e}_2}(\boldsymbol{\xi}) + \xi_3 b^{r-1}_{\mathbf{i}+\mathbf{e}_3}(\boldsymbol{\xi}), \tag{9}$$

where $r = 1, \cdots, d$, $|\mathbf{i}| = d - r$ and $\mathbf{e}_1 = (1, 0, 0)$, $\mathbf{e}_2 = (0, 1, 0)$ and $\mathbf{e}_3 = (0, 0, 1)$.

3 Domain parameterization

Whether in IGA or in FEA, the mesh has to be generated first before performing analysis. In our work, we need to create the Bézier triangular mesh for a given physical domain defined by B-splines boundary. For the design domain defined with arbitrary B-splines boundary, automatic meshing is desired in order to avoid manual meshing or re-meshing. In the present work, the Bézier triangular mesh is automatically generated following the procedure introduced in [23, 24]. The procedure is briefly illustrated in Fig. 1 and described as follows.

Step 1 For a given design domain defined with B-splines boundary of degree d (Figure 1(a)), each B-splines boundary is subdivided into Bézier segments through knots insertion (Figure 1(b)).

Step 2 Construct the polygonal parametric domain $\widehat{\Omega}$ by connecting the end points of the Bézier segments and triangulating the parametric domain $\widehat{\Omega}$ using triangulation scheme (Fig. 1(c)). The only parameter that controls the triangulation process is the maximum mesh size, h. This procedure leads to the triangulation of the parametric domain, $\widehat{T}$.

Step 3 Generate the domain points of degree d in the parametric domain (Figure 1(d)) for each triangle in $\widehat{T}$ based on Eq. (8).

Step 4 Replace boundary control points of $\widehat{T}$ in Fig. 1(d) with the corresponding points of Bézier segments obtained in Step 1. Fig. 1(e) uses a patch to show the replacement process. As shown in Fig. 1(e), the middle control point of boundary line (blue circle) is substituted with the corresponding boundary Bézier control point(red circle). The final Bézier triangular mesh, T, is shown in Fig. 1(f).

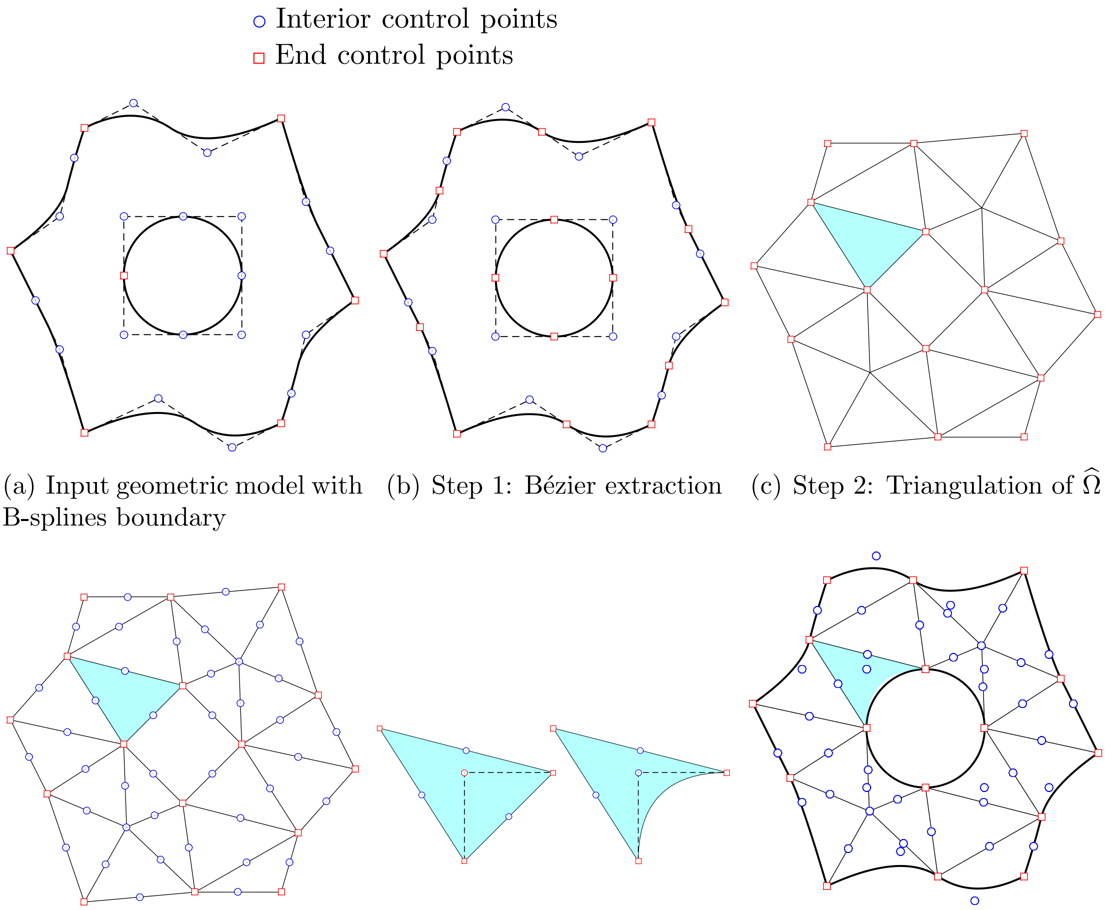

(a) Input geometric model with B-splines boundary

(b) Step 1: Bézier extraction

(c) Step 2: Triangulation of $\widehat{\Omega}$

(d) Step 3: Domain points generation

(e) Step 4: Boundary replacement

(f) Final physical domain

Figure 1: Parameterization of a domain bounded by B-spline curves with Bézier triangles.

4 Parameterization quality of Bézier patches via Jacobian

In our work, we want to guarantee mesh validity even when design boundary deforms significantly. This can be achieved by representing the Jacobian determinant as a Bézier form and guaranteeing those Bézier coefficients to be positive [16, 34, 35].

The Jacobian matrix of $\mathbf{x}(\boldsymbol{\xi})$ given by Eq. (5) is written as

$$\mathbf{J} = \begin{bmatrix} \frac{\partial x}{\partial \xi_1} & \frac{\partial y}{\partial \xi_1} \\ \frac{\partial x}{\partial \xi_2} & \frac{\partial y}{\partial \xi_2} \end{bmatrix}. \tag{10}$$

Based on the Eq. (5), the partial derivatives of a triangular Bézier patch $\mathbf{x}(\boldsymbol{\xi})$ read

$$\begin{aligned} \frac{\partial \mathbf{x}(\boldsymbol{\xi})}{\partial \xi_1} &= d \sum_{|\mathbf{i}|=d-1} \mathbf{p}_{\mathbf{i}+\mathbf{e}_1} B_{\mathbf{i},d-1}(\boldsymbol{\xi}), \\ \frac{\partial \mathbf{x}(\boldsymbol{\xi})}{\partial \xi_2} &= d \sum_{|\mathbf{i}|=d-1} \mathbf{p}_{\mathbf{i}+\mathbf{e}_2} B_{\mathbf{i},d-1}(\boldsymbol{\xi}), \\ \frac{\partial \mathbf{x}(\boldsymbol{\xi})}{\partial \xi_3} &= d \sum_{|\mathbf{i}|=d-1} \mathbf{p}_{\mathbf{i}+\mathbf{e}_3} B_{\mathbf{i},d-1}(\boldsymbol{\xi}). \end{aligned}$$

Then the determinant of Jacobian, $|\mathbf{J}|$, can be written as

$$\begin{aligned} |\mathbf{J}| &= \det[\frac{\partial \mathbf{x}(\boldsymbol{\xi})}{\partial \xi_1} - \frac{\partial \mathbf{x}(\boldsymbol{\xi})}{\partial \xi_3}, \frac{\partial \mathbf{x}(\boldsymbol{\xi})}{\partial \xi_2} - \frac{\partial \mathbf{x}(\boldsymbol{\xi})}{\partial \xi_3}] \\ &= d^2 \sum_{|\mathbf{s}|=2d-2} B_{\mathbf{s},2d-2}(\boldsymbol{\xi}) J_{\mathbf{s}}, \end{aligned} \tag{11}$$

where $J_{\mathbf{s}}$ are the coefficients of the Jacobian determinant and are called Jacobian ordinates in our work. The $J_{\mathbf{s}}$ read

$$J_{\mathbf{s}} = \sum_{\substack{\mathbf{i}_1+\mathbf{i}_2=\mathbf{s} \\ |\mathbf{i}_1|=d-1 \\ |\mathbf{i}_2|=d-1}} \frac{\binom{d-1}{\mathbf{i}_1}\binom{d-1}{\mathbf{i}_2}}{\binom{2d-2}{\mathbf{i}_1+\mathbf{i}_2}} \det[\mathbf{p}_{\mathbf{i}_1+\mathbf{e}_1} - \mathbf{p}_{\mathbf{i}_1+\mathbf{e}_3}, \mathbf{p}_{\mathbf{i}_2+\mathbf{e}_2} - \mathbf{p}_{\mathbf{i}_2+\mathbf{e}_3}]. \tag{12}$$

From Eq. (11) we can know that if all $J_{\mathbf{s}}$ are positive, so is the determinant $|\mathbf{J}|$.

5 Shape optimization

This section describes details of the isogeometric shape optimization based on Bézier triangles. The 2D elasticity problem is studied first to validate the proposed method. Then the method is also applied to design materials with negative Poisson's ratio.

5.1 2D elasticity analysis

The governing equations for 2D elasticity with linear isotropic materials reads

$$\nabla \cdot \boldsymbol{\sigma} + \mathbf{f} = 0 \quad \mathsf{in} \quad \Omega \tag{13a}$$

$$\mathbf{u} = \bar{\mathbf{u}} \quad \mathsf{on} \quad \Gamma_u, \tag{13b}$$

$$\mathbf{t} \equiv \boldsymbol{\sigma} \cdot \mathbf{n} = \bar{\mathbf{t}} \quad \mathsf{on} \quad \Gamma_{\mathsf{t}} \tag{13c}$$

where $\mathbf{f}$ is the body force vector, $\mathbf{t}$ is the traction, and $\mathbf{u}$ is the displacement vector. Γ_t and Γ_u are the boundary where the traction and displacement are specified. $\boldsymbol{\sigma}$ is the stress tensor. In analysis, Eq. (13) leads to the following discrete governing equilibrium equation

$$\mathbf{K}\mathbf{u} = \mathbf{F}, \tag{14}$$

where $\mathbf{K}$, $\mathbf{u}$, and $\mathbf{F}$ are the global stiffness matrix, displacement vector, and force vector, respectively. The stiffness matrix $\mathbf{K}$ and the force vector $\mathbf{F}$ can be assembled from the element stiffness matrix $\mathbf{K}_e$ and the element load vector $\mathbf{F}_e$. $\mathbf{K}_e$ and $\mathbf{F}_e$ read

$$\mathbf{K}_e = \int_{\widehat{\Omega}_e} \mathbf{B}^{\mathsf{T}}\mathbf{D}\mathbf{B}|\mathbf{J}|t_e \mathrm{d}\widehat{\Omega}_0, \tag{15}$$

$$\mathbf{F}_e = \int_{\widehat{\Omega}_e} \mathbf{N}^{\mathsf{T}}\mathbf{f}|\mathbf{J}|t_e \mathrm{d}\widehat{\Omega}_0 + \int_{\widehat{\Gamma}_t} \mathbf{N}^{\mathsf{T}}\mathbf{t}|\mathbf{J}|\mathrm{d}\widehat{\Gamma}_0, \tag{16}$$

where $\mathbf{D}$ is the stress strain matrix, $\mathbf{B}$ is the strain displacement matrix, t_e is the plate element thickness, $\widehat{\Omega}_0$ is the integration parent cell, and $\widehat{\Gamma}_0$ is the traction boundary in $\widehat{\Omega}_0$. The above integrals can be evaluated numerically by applying the Gaussian quadrature rule on the element level.

5.2 Structural shape optimization

In our work, we focus on the development of the optimization method and study a simple structural optimization problem, the minimization of the compliance under a volume constraint. The corresponding optimization formulation reads

$$\min_{\boldsymbol{\alpha}} \quad \mathcal{C}(\boldsymbol{\alpha}, \mathbf{u}(\boldsymbol{\alpha})) = \mathbf{F}^{\mathsf{T}}\mathbf{u} \tag{17a}$$

$$s.t. \quad \mathbf{K}\mathbf{u} = \mathbf{F} \tag{17b}$$

$$g(\boldsymbol{\alpha}) = V/V^{\star} \leq 1, \tag{17c}$$

$$\boldsymbol{\alpha}_{\mathsf{lb}} \leq \boldsymbol{\alpha} \leq \boldsymbol{\alpha}_{\mathsf{ub}} \tag{17d}$$

where $V^{\star}$ is the maximum volume constraint. $\boldsymbol{\alpha}_{\mathsf{lb}}$ and $\boldsymbol{\alpha}_{\mathsf{ub}}$ are the lower and upper bounds of optimization variables. In our implementation, α represents the B-spline control points of design boundaries, and contains the geometric information of the CAD model. Then it is straightforward to link the bounds α_{lb} and α_{ub} to dimensions of the CAD model. Based on the convex property of B-spline curves, the bounds α_{lb} and α_{ub} can be prescribed based on the moving range of design boundaries.

In the work, the coordinates of the B-splines control points of design boundary are chosen as optimization variables. Choosing the control points of B-splines rather than the control points of Bézier curves as optimization variables has many advantages. First, the number of optimization variables would be very small in the first case and the optimization variables would remain the same during the optimization process. Second, the remeshing process becomes very convenient when choosing the control points of B-splines as optimization variables. In this way, we just need to change control points of B-splines and repeat the mesh generation procedure described in Fig. 1. Finally, choosing the control points of B-splines as optimization variables can successfully obviate the need for extraneous filtering [36, 37, 38]. It is because the control points of B-splines themselves can be seen as averages of the Bézier control points for the same boundary [39].

The optimization process will be elaborated in the following through the optimal design of a plate with a hole. The design problem is illustrated in Fig. 15.

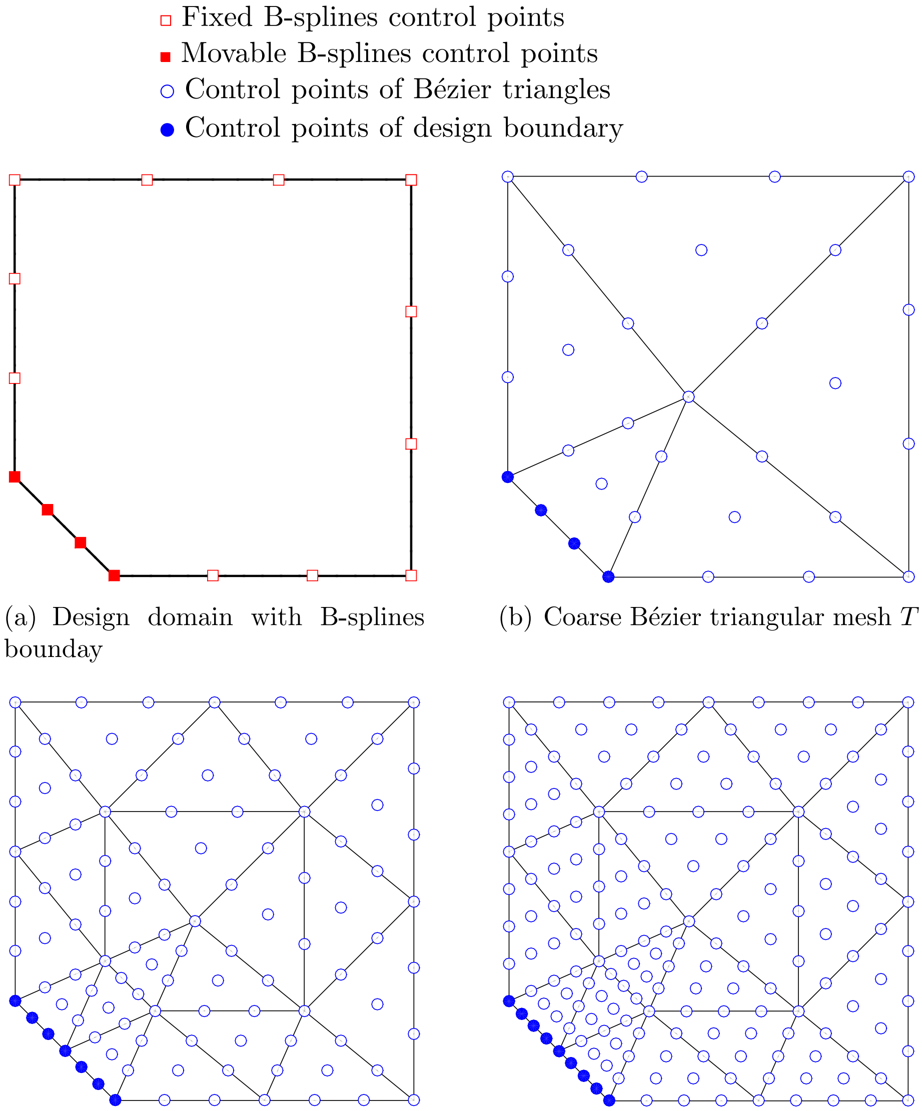
□ Fixed B-splines control points
■ Movable B-splines control points
○ Control points of Bézier triangles
● Control points of design boundary

(a) Design domain with B-splines bounday

(b) Coarse Bézier triangular mesh T

(c) Fine mesh T^* with refinement

(d) Fine mesh T^* with refinement and degree elevation

Figure 2: Bézier triangular mesh generation for a plate with a hole. Only a quarter of the plate is shown.

Mesh generation For a given design problem, the design domain will be defined by B-splines boundary. For the design of a plate with a hole, the B-splines boundary for a quarter of plate is shown in Fig. 2(a). Then a coarse Bézier triangular mesh T (Fig. 2(b)) is generated following the procedures as illustrated in Fig. 1. As the coarse mesh is just used to represent the geometry and check the mesh quality, a small number of Bézier triangles with low degree are created. For the fine mesh T^*, we generally use a large number of triangles of higher degree in order to achieve high analysis accuracy. For Bézier triangles, the fine mesh can be easily generated with refinement and degree elevation from the coarse mesh. Fig. 2(c) shows the fine mesh T^* with once refinement from the coarse mesh in Fig. 2(b) and Fig. 2(d) shows the fine mesh T^* with both refinement and degree elevation.

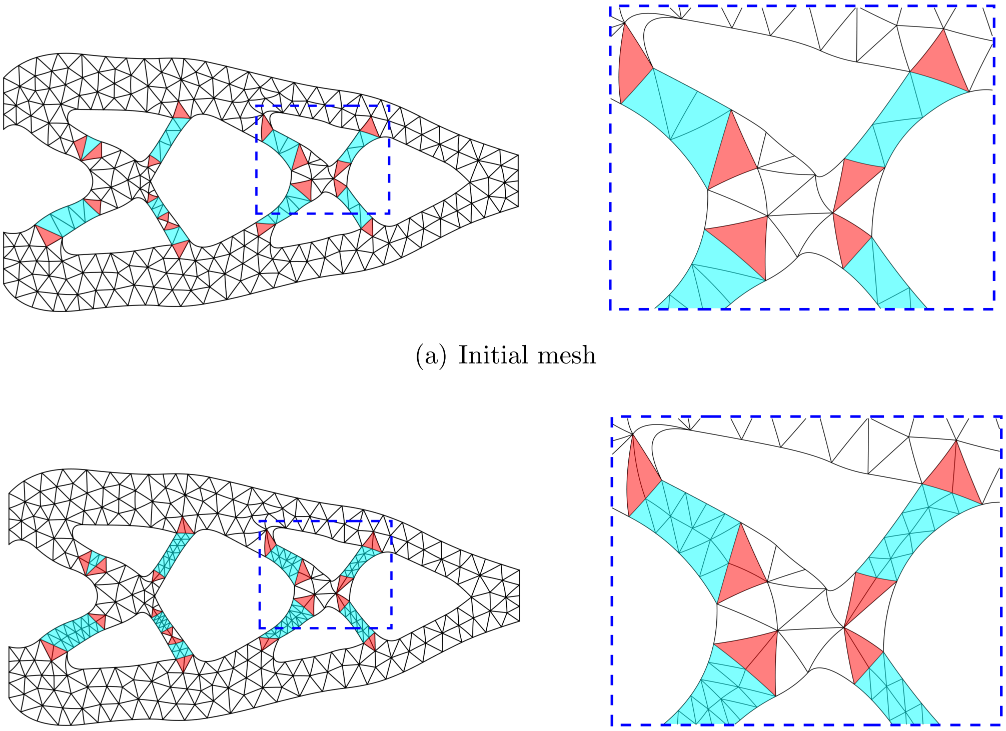

(a) Initial mesh

(b) Locally refined mesh

Figure 3: Local refinement of thin connections. For better analysis accuracy, single-element connections are refined.

In practice, if overly thin connections develop during the optimization process, the generated coarse mesh may contain only one layer of triangles between different design boundaries. This kind of connections are very stiff and may lead to numerical inaccuracy in the analysis. Therefore, we require that at least two layers elements exist in the thin connections. This can be implemented by uniform refinement as discussed above or by applying very small element size. Both methods will lead to a large number of elements and thus extremely increase the computational cost. Due to the use of Bézier triangulation, we can instead just locally refine those triangles that singly connect multiple boundaries. Figure 3(a) shows the initial coarse mesh of an intermediate design of a cantilever with six holes. We can observe that only one layer of triangles exist between holes. If we try to guarantee two layers of triangles in every thin connections, the mesh size has to be extremely small. There exist only two types of this kind of single triangles. For the type I (cyan), all the three vertices of the triangles are on the boundary; for the type II (red), only two vertices are on the boundary and another vertex is in the interior domain. For the type I, we perform uniform h-refinement by connecting edge midpoints to subdivide each triangle into four triangles. For the type II, each triangle

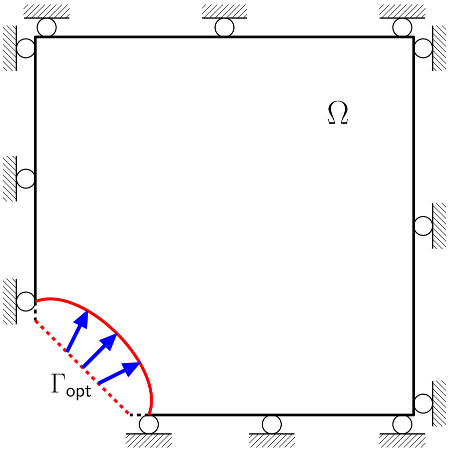

Figure 4: Boundary conditions for the mesh movement problem. The problem is solved based on the coarse mesh T as shown in Fig. 2(b).

is bisected across the edge that connects two different boundaries. The locally refined triangular mesh is shown in 3(b). In this way, two layers of triangles are guaranteed in the thin connections, and the total number of triangles hasn't been dramatically increased. It should be noted that any number of layers of elements can be generated within thin connections by local refinement or uniform refinement. In our implementation, two layers of elements are guaranteed in the thin connections for the coarse mesh through local refinement, and four layers of elements are guaranteed for the fine mesh through further uniform refinement.

Mesh movement As design boundary moves, the movements of the internal control points are determined by solving a pseudo linear elasticity problem [40] based on the coarse mesh T as shown in Fig. 2(b). The boundary conditions for the mesh movement problem are shown in Fig. 4. Compared with the original design problem defined in Fig. 15, only essential boundary conditions are applied in this case and the variation of Bézier control points of the design boundary are imposed as prescribed displacements. The pseudo linear elasticity problem then can be defined as

$$\begin{aligned} \nabla \cdot \boldsymbol{\sigma} = 0 \quad &\text{in} \quad \Omega && \text{(18a)} \\ \mathbf{u} = \delta \widetilde{\mathbf{p}}^B \quad &\text{on} \quad \Gamma_{\text{opt}} \qquad , && \text{(18b)} \\ \mathbf{u} = \mathbf{0} \quad &\text{on} \quad \partial\Omega \backslash \Gamma_{\text{opt}} && \text{(18c)} \end{aligned}$$

where $\delta \widetilde{\mathbf{p}}^B$ defines the variation of control points of the design boundary in the coarse mesh. By solving Eq. (18), the variation of the internal control points in the coarse mesh T is calculated as

$$\delta \widetilde{\mathbf{p}}^I = \mathbf{A} \delta \widetilde{\mathbf{p}}^B, \tag{19}$$

where $\mathbf{A}$ is a linear matrix and is computed in the preprocessing step. In our work, every time a new coarse mesh is generated, the matrix $\mathbf{A}$ will be recalculated.

Mesh quality maintaining As the design boundary is allowed to largely deform, self-intersections of boundary or meshes may occur. As illustrated in Fig. 5(a), as the design boundary moves, self-intersection occurs in the coarse mesh. The corresponding Jacobian

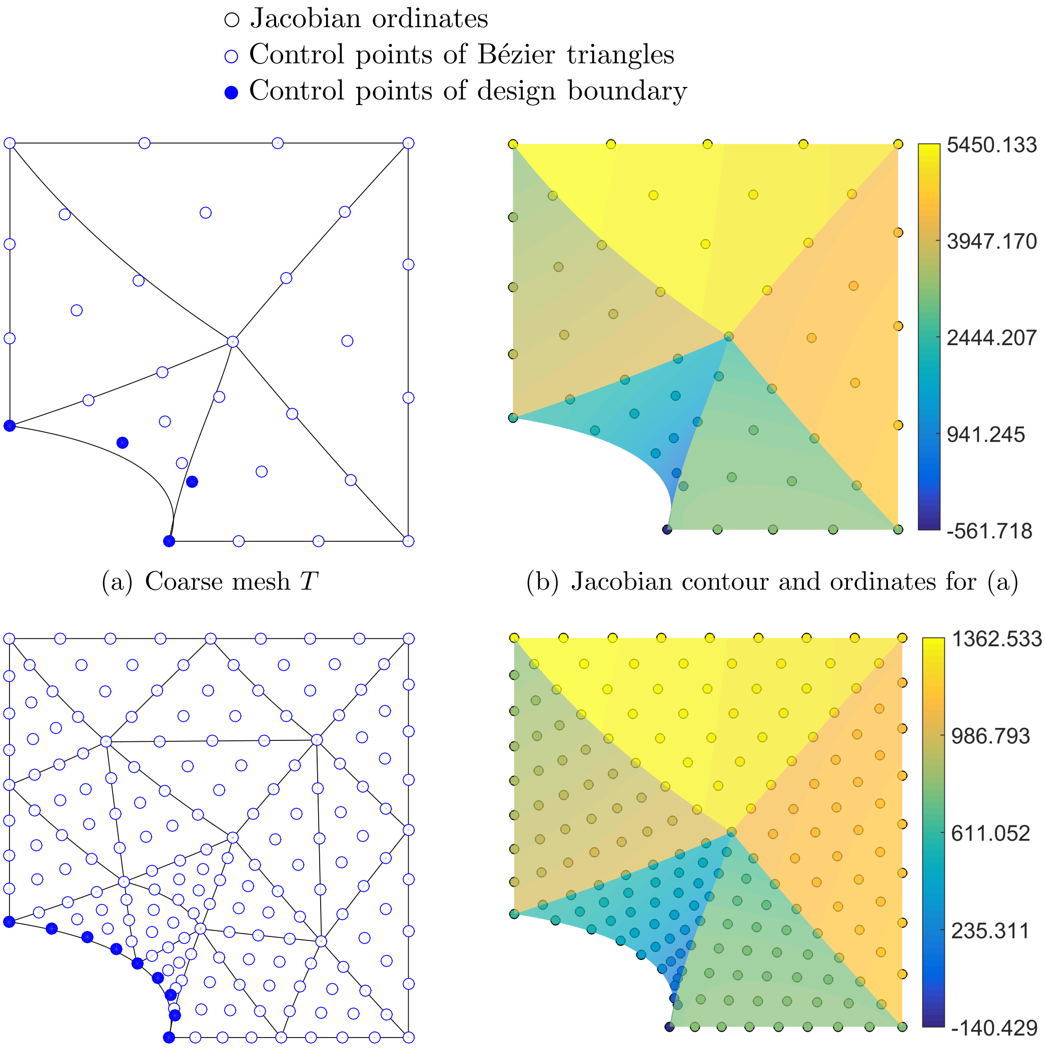

(a) Coarse mesh T

(b) Jacobian contour and ordinates for (a)

(c) Fine mesh T^*

(d) Jacobian contour and ordinates for (c)

Figure 5: Jacobian of the coarse mesh and the fine mesh with self-intersections.

contour and the Jacobian ordinates are shown in Fig. 5(b). For the same geometry model, the fine mesh and the corresponding Jacobian contour and ordinates are shown in Fig. 5(c) and (d), respectively. The number of the Jacobian ordinates of the coarse mesh (Figure 5(b)) and the fine mesh (Figure 5(d)) are 75 and 560 separately. As control points of the fine mesh are linear combinations of those of the coarse mesh, the Jacobian ordinates of the fine mesh also linearly depend on those of the coarse mesh. That is to say, as we have positive Jacobian ordinates of the coarse mesh, the non-negativity of Jacobian ordinates of the fine mesh is automatically guaranteed. Therefore, only the Jacobian ordinates of the coarse mesh can be used to guarantee mesh validity.

If negative Jacobian ordinates appear, the internal control points of the coarse mesh are moved to guarantee a valid parameterization. This can be implemented by solving the following bound problem [16]

$$\max_{\widetilde{\mathbf{p}}^{\mathbf{I}},\gamma} \quad \gamma \tag{20a}$$

$$\text{s.t.} \quad \gamma - J_{\mathbf{s}} \leq 0, \tag{20b}$$

where $\widetilde{\mathbf{p}}^{\mathbf{I}}$ represent the internal control points of the coarse mesh, γ is an auxiliary op-

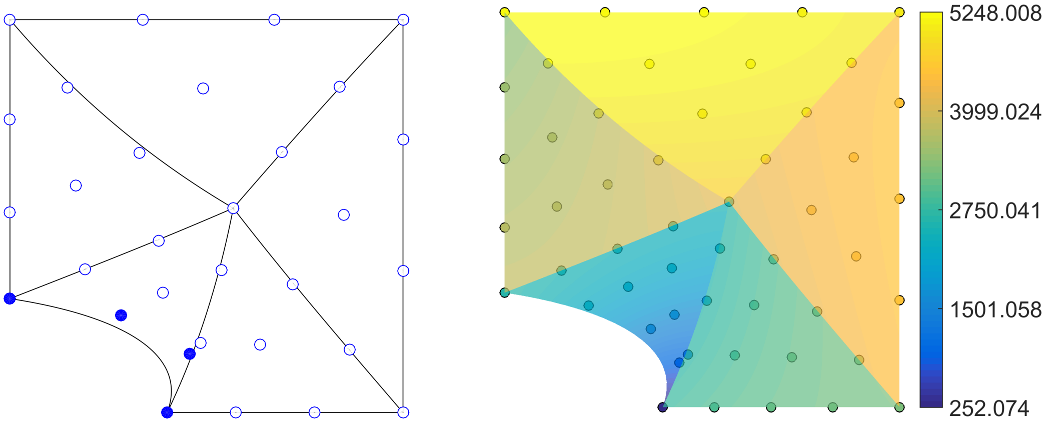

(a) Rectified coarse mesh T

(b) Jacobian contour and ordinates for (a)

Figure 6: Mesh rectification of the invalid mesh in Fig. 5(a).

timization variable and $J_{\mathbf{s}}$ represent the Jacobian ordinates given by Eq. (12). The optimization terminates as soon as γ becomes positive, i.e. a valid parameterization is obtained. The mesh quality obtained in this way does not have to be very high [41]. Despite this drawback, the method provides a simple way to obtain a valid mesh. Furthermore, the optimization problem can converge in a few iterations due to its convexity. This is important to shape optimization as we need to optimize parameterization several times. Figure 6 shows the rectified mesh of the invalid mesh in Fig. 5(a) and corresponding Jacobian contour. The optimization takes only two iterations.

Based on the coarse mesh rather than the fine mesh, the mesh optimization problem Eq. (20) would have less number of optimization variables and constraints, and thus save the computational time. Plus, evaluation of Jacobian ordinates of the coarse mesh is also computationally cheaper. This way to guarantee mesh validity makes a lot sense in the shape optimization. Because we can ensure the mesh quality using the coarse mesh with less computational cost, and simultaneously achieve higher analysis accuracy using the fine mesh.

Although Eq. (20) can rectify the invalid mesh, it cannot avoid sliver elements (i.e. long "thin" elements). The presence of such elements can affect analysis results, and even lead to inaccurate solutions. In order to remove sliver elements in a mesh, another optimization formulation is introduced here to improve mesh quality. First, three criteria are specified to define a sliver element. They are the ratio of the maximum side length to the minimum side length, the minimum interior angle, and the maximum interior angle. In our implementation, the threshold values for these three criteria are 20, 5 degrees and 175 degrees, respectively. If any of these three criteria are violated, an element will be determined as a sliver element.

The interior angles of Bézier triangles can be explicitly controlled. As shown in Fig. 7, the interior angle between two Bézier edges can be represented by their control points. The relationship between θ and the vectors $\mathbf{P}_0\mathbf{P}_1$ and $\mathbf{Q}_0\mathbf{Q}_1$ reads

$$\cos\theta = \frac{\mathbf{P}_0\mathbf{P}_1 \cdot \mathbf{Q}_0\mathbf{Q}_1}{||\mathbf{P}_0\mathbf{P}_1||||\mathbf{Q}_0\mathbf{Q}_1||}. \tag{21}$$

Then the angle constraints can be imposed as

$$\cos\theta \leq \cos\theta_l, \cos\theta \geq \cos\theta_u, \tag{22}$$

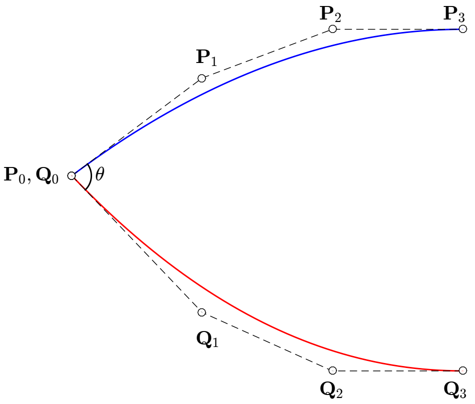

Figure 7: Angle between two Bézier curves.

where θ represents the interior angles for every element, and θ_l and θ_u are the prescribed lower and upper bounds, respectively.

For Bézier triangles, only the angle constraints Eq. (22) can not suppress large aspect ratio of elements, i.e. long 'thin' elements. In practice, it turns out these elements can be suppressed by approximating a conformal map. Therefore, in our implementation, the Winslow functional [42] is minimized to further improve the parameterization quality. The Winslow functional is defined as

$$W = \frac{tr((\mathbf{J})^T \mathbf{J})}{\sqrt{\det(\mathbf{J}^T \mathbf{J})}}. \tag{23}$$

As W is minimized, $\mathbf{J}^T\mathbf{J}$ would be "as identically diagonal as possible" [43], and J would be almost a combination of scaling and rotation transformations.

Hence, the optimization problem to eliminate sliver elements can be defined as

$$\begin{aligned}
\min_{\widetilde{\mathbf{p}}^{\mathbf{I}}} \quad & \int_0^1 \int_0^1 W(\widetilde{\mathbf{p}}) \mathrm{d}\xi_1 \mathrm{d}\xi_2 && \text{(24a)}\\
\text{s.t.} \quad & \cos(\theta) \leq \cos(\theta_l) && \text{(24b)}\\
& \cos(\theta) \geq \cos(\theta_u) && \text{(24c)}\\
& J_{\mathbf{s}} \geq 0. && \text{(24d)}
\end{aligned}$$

It should be noted that the angle constraints in Eq. (24) are imposed based on the assumption that the mesh is valid. Therefore, Jacobian constraints Eq. (24d) are also applied to obtain a valid parameterization. The Winslow functional is widely used to improve parameterization quality in isogeometric analysis, e.g. [35, 15]. More information on parameterization quality in isogeometric analysis can also be found in [44].

Figure 8 illustrates the elimination of sliver elements in a mesh without highly distorted edges. Figure 8(a) shows a mesh with sliver elements, i.e. I,II and III. The element I has the minimum angle 3.7 degrees. The elements II and III have the minimum angle 3.0 degrees, and the ratio of the maximum side length to the minimum side length 23.57. We solve Eq. (24) to remove these sliver elements. The optimized mesh is shown in Fig. 8(b), for which the minimum angle is 19.66 degrees. It can be also observed that there are no long "thin" elements in the optimized mesh.

Then we investigate another mesh as shown in Fig. 9(a). This time the design boundary is highly distorted. The minimum interior angle happens in the element I,

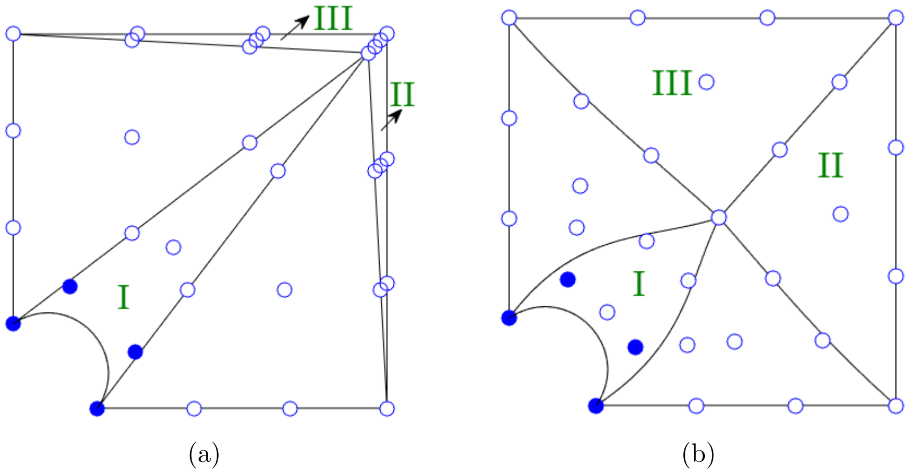

Figure 8: Elimination of sliver elements in a mesh without highly distorted boundaries. (a) A mesh with sliver elements, (b) optimized mesh.

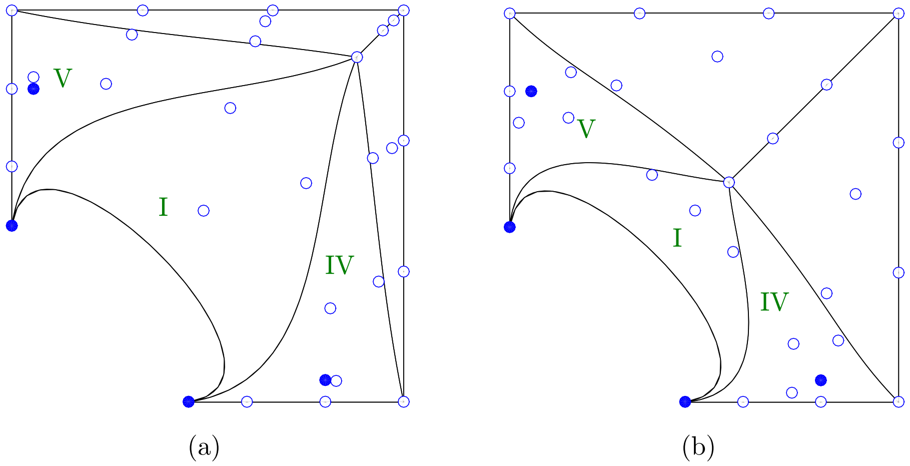

Figure 9: Elimination of sliver elements in a mesh with highly distorted boundaries. (a) A mesh with sliver elements, (b) optimized mesh.

and it is 1.78 degrees. The optimized mesh with Eq. (24) is shown in Fig. 9(b). Angle constraints are not satisfied in this case. For mesh in Fig. 9(b), the minimum angle happens in the element I, and it is 4 degrees, which is still smaller than the given lower bound $\theta_l = 5°$. The optimization problem Eq. (24) can not find solution in this case. It is because the intersection angle between the boundary of the internal hole and the adjacent boundaries are just 9 degrees, but there are two elements at the corners. Therefore, as design boundaries are highly distorted, solving the optimization problem Eq. (24) may not guarantee angle constraints. In this case, we resort to remeshing to improve parameterization.

The regenerated mesh for the highly-distored mesh in Fig. 9(a) is shown in Fig. 10(a). The Jacobian contour of Fig. 10(a) is shown in Fig. 10(b). It can be observed that after remeshing, the mesh is valid, and there are no sliver elements. The minimum interior angle is 9 degrees, which just equals to the intersection angle between the internal hole and the adjacent boundaries. In practice, for the regenerated mesh, if there are a couple of elements at the sharp corners, we just locally modify the mesh so that angle constraints can be satisfied.

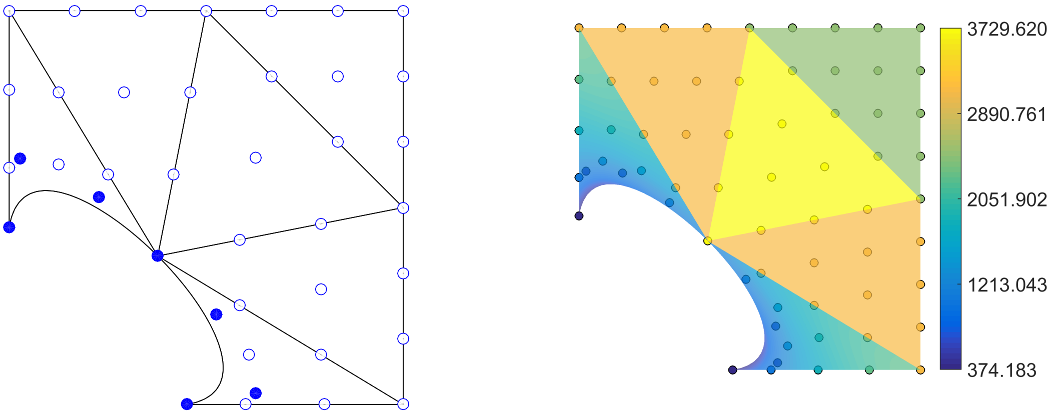

(a) Regenerated coarse mesh T

(b) Jacobian contour and ordinates for (c)

Figure 10: Remeshing a distorted mesh.

In our implementation, if Eq. (24) can not obtain high quality mesh in the given iterations, e.g. 30, we do remeshing to improve parameterization. The criteria used to evaluate mesh quality are the positivity of Jacobian ordinates and those criteria used for judging sliver elements. It should be noted that, in order to impose interior angle constraints, the angle between the adjacent B-splines boundaries should satisfy angle constraints first. The intersection angles between the adjacent B-splines boundaries can also be explicitly derived as in Eq. (21), and added to the optimization formulation Eq. (17) as constraints. The number of these angle constraints are at the same level as the number of B-spline boundaries. Therefore, only a few angle constraints are added into the optimization formulation Eq. (17), and they have little effect on computational cost.

Boundary distance control In shape optimization, as design boundaries move, intersection may happen. Also, to make the optimized design manufacturable or avoid stress concentration, the minimum thickness of connections should be controlled. In our work, the distance between two design boundaries is explicitly controlled. The idea is to represent the distance function between two curves as a B-spline or Bézier form and directly operate on the corresponding coefficients. In our implementation, we first extract Bézier segments from B-splines boundary and then represent the squared distance between each pair of Bézier curves as a Bézier form.

Given two Bézier curves, $\mathbf{C}_1(u)$ and $\mathbf{C}_2(v)$, of degree m and n

$$\mathbf{C}_1(u) = \sum_{|\mathbf{i}|=m} \mathbf{P}_\mathbf{i} B_{\mathbf{i},m}(u), \quad u \in [0,1] \tag{25}$$

$$\mathbf{C}_2(v) = \sum_{|\mathbf{j}|=n} \mathbf{Q}_\mathbf{j} B_{\mathbf{j},n}(v), \quad v \in [0,1], \tag{26}$$

the squared distance between $\mathbf{C}_1(u)$ and $\mathbf{C}_2(v)$ reads

$$S(u,v) = \left(\sum_{|\mathbf{i}|=m} \mathbf{P}_\mathbf{i} B_{\mathbf{i},m}(u) - \sum_{|\mathbf{j}|=n} \mathbf{Q}_\mathbf{j} B_{\mathbf{j},n}(v) \right)^2 = \sum_{|\mathbf{r}|=2m} \sum_{|\mathbf{s}|=2n} D_{\mathbf{r},\mathbf{s}} B_{\mathbf{r},2m}(u) B_{\mathbf{s},2n}(v), \tag{27}$$

where $D_{\mathbf{r},\mathbf{s}}$ represent the squared distance ordinates. The derivation of the Bézier form Eq. (27) is explained in Appendix. The readers can also refer to [45, 46] for details.

Due to the convex hull property of the Bézier representation, we can control the minimum thickness of connections by the following constraints

$$D_{\mathbf{r},\mathbf{s}} \geq D_{\min}. \tag{28}$$

where $D_{\min}$ is the given limit of the squared distance. In practice, each knot span of a B-spline boundary corresponds to one Bézier segment, and we need to derive the squared distance between each pair of Bézier segments respectively on different B-splines curves. From Eq. (27), we know that for two Bézier curves of degree m and n, there will be $(2m + 1) \times (2n + 1)$ number of distance ordinates. Hence the number of the distance ordinates will be huge as a large number of B-spline curves are employed to represent the design domain. Then considering the point-wise distance constraints Eq. (28) in the optimization will be computationally expensive.

In our implementation, instead of incorporating the constraints Eq. (28) into the optimization formulation, we only check whether the constraints will be violated or not. If violated, the step length of the optimization variables is reduced to satisfy the constraints Eq. (28). Figure 11 illustrates this process. As the design boundary $\mathbf{C}_1$ is updated by $\mathbf{C}_1 + \Delta\mathbf{C}_1$, if intersection happens, then the updated $\mathbf{C}_1$ is moved back with a smaller step length $\beta\Delta\mathbf{C}_1$. In practice, we just need to modify the optimization variables that are related to the violated distance ordinates. This strategy to consider the distance constraints is easy to implement and computationally cheap. It has been proved to be efficient in distance control.

Flowchart In the end, the procedures of the proposed optimization method are briefly summarized by the flow chart in Fig. 12. For a given geometry defined by the B-splines boundary, the coordinates of control points of B-splines for the user-specified design boundary are set as optimization variables, $\boldsymbol{\alpha}$. Each time the design boundary is updated, the distance constraints Eq. (28) are checked first to prevent intersections or guarantee the minimum thickness of structural connections. Then a coarse triangular Bézier mesh, T, is automatically generated following the procedure discussed in Section 3. As the movements of boundary control points in T linearly depend on $\boldsymbol{\alpha}$ through knots insertion, the variation of the internal control points in T is determined by solving the

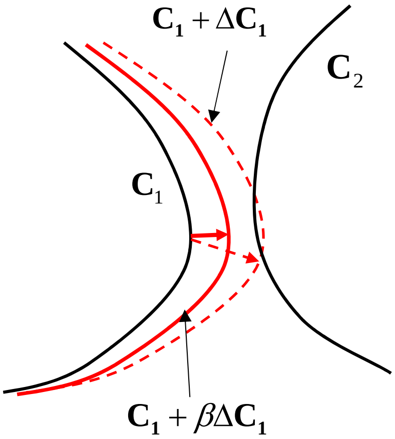
$\mathbf{C}_1 + \Delta\mathbf{C}_1$
$\mathbf{C}_2$
$\mathbf{C}_1$
$\mathbf{C}_1 + \beta\Delta\mathbf{C}_1$

Figure 11: Determination of the step length after the distance constraints Eq. (28) are violated.

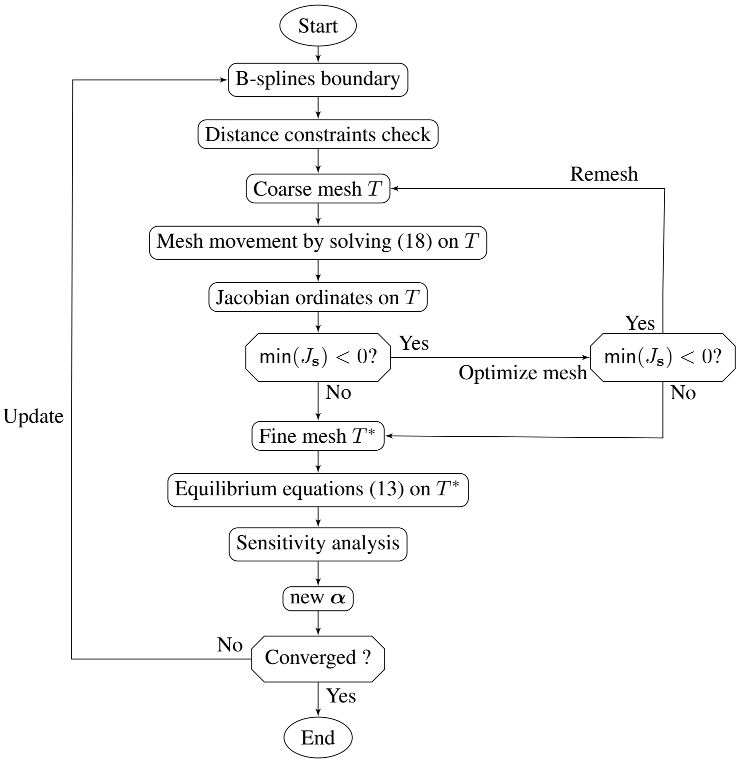
Start
B-splines boundary
Distance constraints check
Coarse mesh T
Remesh
Mesh movement by solving (18) on T
Jacobian ordinates on T
$\min(J_{\mathbf{s}}) < 0$?
Yes
Optimize mesh
Yes
$\min(J_{\mathbf{s}}) < 0$?
No
No
Update
Fine mesh T^*
Equilibrium equations (13) on T^*
Sensitivity analysis
new $\boldsymbol{\alpha}$
No
Converged ?
Yes
End

Figure 12: The flow chart of the optimization process.

pseudo linear elasticity equation Eq. (18). If the coarse mesh is invalid, the mesh would be rectified by solving the mesh optimization problem Eq. (24). If the mesh rectification process cannot obtain valid parameterization within 30 iterations, the coarse mesh would be regenerated. The remeshing process just repeats the mesh generation process as discussed in Section 3. After the coarse mesh becomes valid, a corresponding fine mesh T^* is produced by elevating degree or refining mesh. The optimization variables are updated based on the sensitivity information obtained from solving the linear equations Eq. (13) on the fine mesh T^*.

5.3 Auxetic materials design

The proposed shape optimization method is also used to design materials with negative Poisson's ratio. In the following, the strain energy based method [47] is first introduced to predict the effective elastic tensor of a unit cell. Then, the optimization formulation to design NPR materials is presented.

5.3.1 Prediction of effective elastic tensor of a unit cell

For a complex material with a periodic micro structure, we can use a unit cell, which is the smallest repetitive unit of the material, to represent the material. The material behaviors of the unit cell can be characterized by the average stress $\bar{\sigma}_{ij}$ and the average strain $\bar{\varepsilon}_{kl}$ in a homogeneous medium. Considering linear elasticity, the constitutive law between $\bar{\sigma}_{ij}$ and $\bar{\varepsilon}_{kl}$ is governed by the generalized Hooke's law

$$\bar{\sigma}_{ij} = C^H_{ijkl}\bar{\varepsilon}_{kl}, \tag{29}$$

where C^H_{ijkl} is the homogenized elastic tensor. For a 2D orthotropic material, Eq. (29) can be rewritten as

$$\begin{bmatrix}\bar{\sigma}_{11}\\ \bar{\sigma}_{22}\\ \bar{\sigma}_{12}\end{bmatrix} = \begin{bmatrix}C^H_{1111} & C^H_{1122} & 0\\ C^H_{2211} & C^H_{2222} & 0\\ 0 & 0 & C^H_{1212}\end{bmatrix}\begin{bmatrix}\bar{\varepsilon}_{11}\\ \bar{\varepsilon}_{22}\\ 2\bar{\varepsilon}_{12}\end{bmatrix}. \tag{30}$$

The effective elastic tensor C^H can be calculated by the standard homogenization approach [48, 49] and the strain energy method [47] for the unit cell. Compared with the homogenization method, the strain energy method is relatively simple to implement. The basis of the method is that the strain energy of the homogeneous medium, $U^H = \frac{1}{2}V\bar{\sigma}_{ij}\cdot\bar{\varepsilon}_{kl}$, and the strain energy of the unit cell, $U = \frac{1}{2}\int_\Omega \sigma_{ij}\varepsilon_{kl}\mathrm{d}\Omega$, are identical. That is

$$\frac{1}{2}V\bar{\sigma}_{ij}\cdot\bar{\varepsilon}_{ij} = \frac{1}{2}\int_\Omega \sigma_{ij}\varepsilon_{kl}\mathrm{d}\Omega, \tag{31}$$

where V is the volume of the unit cell. Then by selecting $\bar{\varepsilon}_{ij}$, the effective material properties can be represented as the strain energy functionals of the unit cell under different loading conditions [47, 50].

Since there are four independent constants in C^H for the 2D orthotropic material, four loading conditions are needed. For the unit cell with symmetric microstructure as shown in Fig. 13(a), only a quarter of the unit cell is considered. Figure 13(b)-(e) define these four loading conditions.

The first load case in Fig. 13(b) corresponds to the average strain $\bar{\varepsilon}_{kl} = [1\ 0\ 0]^{\mathrm{T}}$. From Eq. (30) and Eq. (31), we calculate the strain energy of the homogeneous medium as

$$U^H_{1111} = \frac{V}{2}\begin{bmatrix}1\\0\\0\end{bmatrix}^T\begin{bmatrix}C^H_{1111} & C^H_{1122} & 0\\ C^H_{2211} & C^H_{2222} & 0\\ 0 & 0 & C^H_{1212}\end{bmatrix}\begin{bmatrix}1\\0\\0\end{bmatrix} = \frac{V}{2}C^H_{1111}, \tag{32}$$

and the strain energy of the unit cell under the loading condition in Fig. 13(b) as

$$U_{1111} = \frac{1}{2}\int_\Omega \mathbf{u}_e^T\mathbf{K}_e\mathbf{u}_e\mathrm{d}\Omega. \tag{33}$$

Then from Eq. (31) we have

$$C^H_{1111} = \frac{2}{V}U_{1111}. \tag{34}$$

Similarly, the load cases in Fig. 13(c) and Fig. 13(d) define the strain state $\bar{\varepsilon}_{kl} = [0\ 1\ 0]^{\mathrm{T}}$ and $\bar{\varepsilon}_{kl} = [0\ 0\ \frac{1}{2}]^{\mathrm{T}}$, respectively. And C^H_{2222} and C^H_{1212} can be calculated as

$$C^H_{2222} = \frac{2}{V}U_{2222}, \tag{35}$$

and

$$C^H_{1212} = \frac{2}{V}U_{1212}, \tag{36}$$

where U_{2222} and U_{1212} are the strain energy of the unit cell under the loading conditions in Fig. 13(c) and Fig. 13(d), respectively.

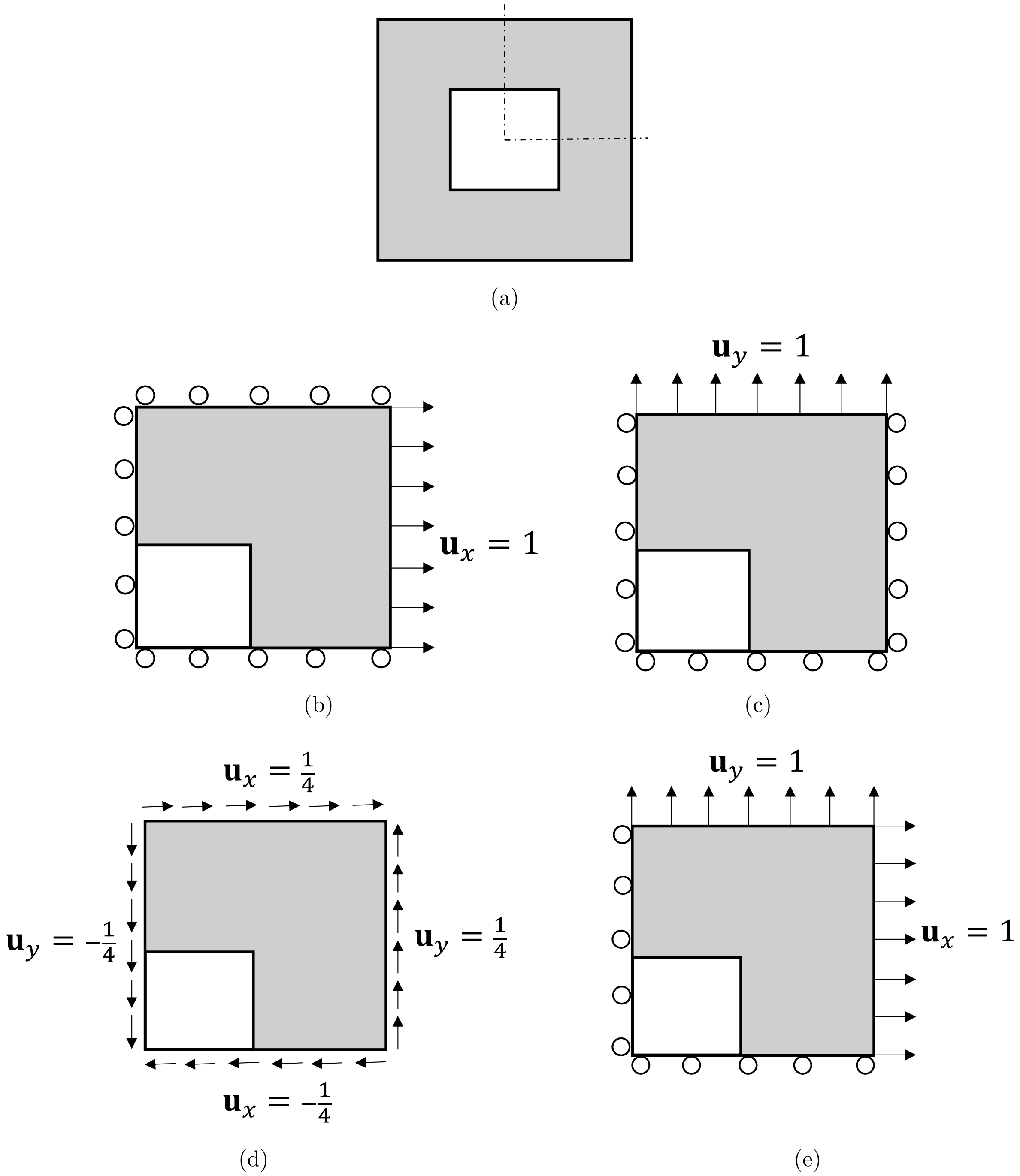

(a)
$\mathbf{u}_x = 1$
(b)
$\mathbf{u}_y = 1$
(c)
$\mathbf{u}_x = \frac{1}{4}$
$\mathbf{u}_y = -\frac{1}{4}$
$\mathbf{u}_y = \frac{1}{4}$
$\mathbf{u}_x = -\frac{1}{4}$
(d)
$\mathbf{u}_y = 1$
$\mathbf{u}_x = 1$
(e)

Figure 13: Unit cell and boundary conditions of the 1/4 unit cell. (a) Unit cell. (b) Load case 1. (c) Load case 2. (d) Load case 3. (e) Load case 4.

The fourth load case in Fig. 13(e) corresponds to the average strain state $\bar{\varepsilon}_{kl} = [1\ 1\ 0]^{\mathrm{T}}$. Then from Eq. (31) and Eq. (30), we have

$$\begin{aligned} U_{1122}^{H} &= \frac{V}{2}\begin{bmatrix}1\\1\\0\end{bmatrix}^{T}\begin{bmatrix}C_{1111}^{H} & C_{1122}^{H} & 0\\ C_{2211}^{H} & C_{2222}^{H} & 0\\ 0 & 0 & C_{1212}^{H}\end{bmatrix}\begin{bmatrix}1\\1\\0\end{bmatrix}\\ &= \frac{V}{2}(C_{1111}^{H}+C_{1122}^{H}+C_{2211}^{H}+C_{2222}^{H})\\ &= U_{1122} \end{aligned} \tag{37}$$

Considering Eq. (34), Eq. (35) and Eq. (37), we have

$$C_{1122}^{H} = \frac{1}{V}(U_{1122} - U_{1111} - U_{2222}). \tag{38}$$

5.3.2 Optimization formulation of NPR materials design

For a given material with periodic microstructure, the described strain energy method can be employed to evaluate the material properties. In our work, the proposed isogeometric shape optimization method is extended to design materials with NPR. The optimization formulation is formulated as

$$\min_{\boldsymbol{\alpha}} \quad \mathcal{J} = \sum_{i,j,k,l} \omega_{ijkl}(C_{ijkl}^{H} - C_{ijkl}^{\star})^2 \tag{39a}$$

$$\text{s.t.} \quad \mathbf{K}\mathbf{u}^{(q)} = \mathbf{F}^{(\mathbf{q})}\ (q = 1, 2, 4) \tag{39b}$$

$$g(\boldsymbol{\alpha}) = V/V^{\star} \leq 1 \tag{39c}$$

$$\boldsymbol{\alpha}_{\mathsf{lb}} \leq \boldsymbol{\alpha} \leq \boldsymbol{\alpha}_{\mathsf{ub}}, \tag{39d}$$

where C_{ijkl}^{H} and $C_{ijkl}^{\star}$ are the calculated and target elastic tensors, respectively. ω_{ijkl} are the weights associated with constants in the tensor. q represent the load cases defined in Fig. 13. For NPR materials design, only C_{1111}^{H}, C_{1122}^{H} and C_{1122}^{H} are considered in the objective function. Therefore, during the shape optimization, only three state equations corresponding to the load cases defined in Fig. 13(b), (c) and (e) are solved.

6 Sensitivity analysis

Sensitivity analysis is a necessary part in the gradient-based optimization algorithm. In the present work, the shape sensitivities of the structural compliance with respect to the control points of the B-splines boundary are analytically derived. It reads

$$\frac{\partial \mathcal{C}}{\partial \boldsymbol{\alpha}} = \frac{\partial \mathbf{F}^{\mathsf{T}}}{\partial \boldsymbol{\alpha}}\mathbf{u} + \mathbf{F}^{\mathsf{T}}\frac{\partial \mathbf{u}}{\partial \boldsymbol{\alpha}}. \tag{40}$$

Considering the equilibrium equation $\mathbf{Ku} = \mathbf{F}$, the Eq. (40) can be further written as

$$\begin{aligned} \frac{\partial \mathcal{C}}{\partial \boldsymbol{\alpha}} &= 2\frac{\partial \mathbf{F}^{\mathsf{T}}}{\partial \boldsymbol{\alpha}}\mathbf{u} - \mathbf{u}^{\mathsf{T}}\frac{\partial \mathbf{K}}{\partial \boldsymbol{\alpha}}\mathbf{u}\\ &= \sum_{e=1}^{N}\left(2\frac{\partial \mathbf{F}_e^{\mathsf{T}}}{\partial \boldsymbol{\alpha}}\mathbf{u}_e - \mathbf{u}_e^{\mathsf{T}}\frac{\partial \mathbf{K}_e}{\partial \boldsymbol{\alpha}}\mathbf{u}_e\right), \end{aligned} \tag{41}$$

where $\boldsymbol{\alpha}$ are the coordinates of the control points of B-splines boundary. The lower case e symbols indicate the element wise quantities and N is the total number of finite elements.

As stated in Eq. (41), to calculate the sensitivity of the compliance, we just need to determine the terms $\frac{\partial \mathbf{K}_e}{\partial \boldsymbol{\alpha}}$ and $\frac{\partial \mathbf{F}_e}{\partial \boldsymbol{\alpha}}$. In the work, $\frac{\partial \mathbf{K}_e}{\partial \boldsymbol{\alpha}}$ and $\frac{\partial \mathbf{F}_e}{\partial \boldsymbol{\alpha}}$ are derived by using the chain rule. First, the derivative of $\mathbf{K}_e$ and $\mathbf{F}_e$ with respect to the coordinates of the control points of the fine mesh, $\mathbf{p}$, is calculated by following the procedures proposed in [11]. Then the nodal sensitivities of $\mathbf{p}$ with respect to the optimization variables $\boldsymbol{\alpha}$ will be given. As shown in Fig. 14, if the B-splines control points $\mathbf{c}_1$ changes, the control points of Bézier triangles in the coarse and fine mesh will change accordingly. Since the boundary control points of the coarse mesh, $\widetilde{\mathbf{p}}^B$, are obtained from B-splines control points through knots insertion, $\frac{\partial \widetilde{\mathbf{p}}^B}{\partial \boldsymbol{\alpha}}$ can be directly derived. Then the derivative of the internal control points in the coarse mesh, $\widetilde{\mathbf{p}}^I$, with respect to $\widetilde{\mathbf{p}}^B$ can be evaluated based on Eq. (19). Finally, since both degree elevation and refinement are linear manipulations, the derivative $\frac{\partial \mathbf{p}}{\partial \widetilde{\mathbf{p}}}$ can also be easily obtained.

6.1 Shape sensitivities based on the fine mesh

Derived from Eq. (15), the sensitivity of the element stiffness matrix $\mathbf{K}_e$ with respect to the s-th optimization variable α_s reads

$$\frac{\partial \mathbf{K}_e}{\partial \mathbf{p}_s} = \int_{\widehat{\Omega}_e} \frac{\partial \mathbf{B}^\mathsf{T}}{\partial \alpha_s} \mathbf{D}\mathbf{B}|\mathbf{J}|t_e + \mathbf{B}^\mathsf{T}\mathbf{D}\frac{\partial \mathbf{B}}{\partial \alpha_s}|\mathbf{J}|t_e + \mathbf{B}^\mathsf{T}\mathbf{D}\mathbf{B}\frac{\partial |\mathbf{J}|}{\partial \alpha_s} t_e \mathrm{d}\widehat{\Omega}. \tag{42}$$

Likewise, according to Eq. (16), the derivative of the element load vector $\mathbf{F}_e$ can be written as

$$\begin{aligned}\frac{\partial \mathbf{F}_e}{\partial \mathbf{p}_s} = &\int_{\widehat{\Omega}_e} \frac{\partial \mathbf{N}^\mathsf{T}}{\partial \alpha_s}\mathbf{f}|\mathbf{J}| + \mathbf{N}^\mathsf{T}\frac{\partial \mathbf{f}}{\partial \mathbf{x}}\frac{\partial \mathbf{x}}{\partial \alpha_s}|\mathbf{J}| + \mathbf{N}^\mathsf{T}\mathbf{f}\frac{\partial |\mathbf{J}|}{\partial \alpha_s} t_e \mathrm{d}\widehat{\Omega} \\ &+ \int_{\widehat{\Gamma}_t} \frac{\partial \mathbf{N}^\mathsf{T}}{\partial \alpha_s}\mathbf{t}|\mathbf{J}| + \mathbf{N}^\mathsf{T}\frac{\partial \mathbf{t}}{\partial \mathbf{x}}\frac{\partial \mathbf{x}}{\partial \alpha_s}|\mathbf{J}| + \mathbf{N}^\mathsf{T}\mathbf{t}\frac{\partial |\mathbf{J}|}{\partial \alpha_s} \mathrm{d}\widehat{\Gamma}.\end{aligned} \tag{43}$$

In Eq. (43), $\frac{\partial \mathbf{f}}{\partial \mathbf{x}}$ and $\frac{\partial \mathbf{t}}{\partial \mathbf{x}}$ appear because the body force $\mathbf{f}$ and the traction $\mathbf{t}$ may depend on locations. The term $\frac{\partial \mathbf{N}^\mathsf{T}}{\partial \alpha_s}$ vanishes as the optimization of weights is not considered. So the left terms are $\frac{\partial \mathbf{B}}{\partial \alpha_s}$, $\frac{\partial |\mathbf{J}|}{\partial \alpha_s}$ and $\frac{\partial \mathbf{x}}{\partial \alpha_s}$, which will be evaluated following the procedures proposed in [11]. Let us define an additional matrices $\mathbf{G}$ as

$$\mathbf{G} = \begin{bmatrix} \frac{\partial N_1}{\partial x} & \frac{\partial N_2}{\partial x} & \cdots & \frac{\partial N_{nc}}{\partial x} \\ \frac{\partial N_1}{\partial y} & \frac{\partial N_2}{\partial y} & \cdots & \frac{\partial N_{nc}}{\partial y} \end{bmatrix}.$$

Then we have

$$\frac{\partial |\mathbf{J}|}{\partial \alpha_s} = |\mathbf{J}|\mathsf{tr}(\mathbf{G}\frac{\partial \mathbf{p}}{\partial \alpha_s}), \tag{44}$$

$$\frac{\partial \mathbf{G}}{\partial \alpha_s} = -\mathbf{G}\frac{\partial \mathbf{p}}{\partial \alpha_s}\mathbf{G}, \tag{45}$$

$$\frac{\partial \mathbf{x}}{\partial \alpha_s} = \mathbf{N}^\mathbf{T}\frac{\partial \mathbf{p}}{\partial \alpha_s}. \tag{46}$$

After $\frac{\partial \mathbf{G}}{\partial \alpha_s}$ is computed, the term $\frac{\partial \mathbf{B}}{\partial \alpha_s}$ can be directly derived. In above equations, $\frac{\partial \mathbf{p}}{\partial \alpha_s}$ (n_c by 2) represents the nodal sensitivity and it will be calculated in the following subsections.

6.2 Sensitivity propagation from the coarse mesh to the fine mesh

As the coarse Bézier triangular mesh is automatically generated for a given CAD model defined by B-splines boundary, we obtain the fine mesh through degree elevation and mesh refinement. The control points for the coarse mesh are denoted as $\widetilde{\mathbf{p}}$.

Degree elevation Generally, we just use lower order(e.g. quadratic) Bézier patches to define the geometric model but higher order patches for analysis. For example, we use $d+1$ degree Bézier patches for the fine mesh and d degree for the coarse mesh. Because the same patch is defined, then it reads[33]

$$\sum_{|\mathbf{i}|=d} \widetilde{\mathbf{p}}_{\mathbf{i}} B_{\mathbf{i},d}(\boldsymbol{\xi}) = \sum_{|\mathbf{i}|=d+1} \mathbf{p}_{\mathbf{i}} B_{\mathbf{i},d+1}(\boldsymbol{\xi}), \tag{47}$$

with

$$\mathbf{p}_{\mathbf{i}} = \frac{1}{d+1}[i\widetilde{\mathbf{p}}_{\mathbf{i}-\mathbf{e}_1} + j\widetilde{\mathbf{p}}_{\mathbf{i}-\mathbf{e}_2} + k\widetilde{\mathbf{p}}_{\mathbf{i}-\mathbf{e}_3}]. \tag{48}$$

Derived from Eq. (48), then the sensitivities from control points of the coarse mesh to those of the fine mesh are calculated by

$$\frac{\partial \mathbf{p}_{\mathbf{i}}}{\partial \alpha_s} = \frac{i}{d+1}\frac{\partial \widetilde{\mathbf{p}}_{\mathbf{i}-\mathbf{e}_1}}{\partial \alpha_s}, \quad \frac{\partial \mathbf{p}_{\mathbf{i}}}{\partial \alpha_s} = \frac{j}{d+1}\frac{\partial \widetilde{\mathbf{p}}_{\mathbf{i}-\mathbf{e}_2}}{\partial \alpha_s}, \quad \frac{\partial \mathbf{p}_{\mathbf{i}}}{\partial \alpha_s} = \frac{k}{d+1}\frac{\partial \widetilde{\mathbf{p}}_{\mathbf{i}-\mathbf{e}_3}}{\partial \alpha_s}. \tag{49}$$

Note that this degree elevation can be repeated to get higher order Bézier patches.

Mesh refinement For the uniform refinement process, each triangle in the coarse mesh is divided into four triangles in the fine mesh as shown in Fig. 14. And each control point in the fine mesh is a linear combination of the control points in the coarse mesh [51] and can be evaluated using the de Casteljau algorithm stated in Eq. (9). Then the control points of the fine mesh can be expressed as

$$\mathbf{p}_{\mathbf{j}} = \sum_{\mathbf{i}} C_{\mathbf{j},\mathbf{i}} \widetilde{\mathbf{p}}_{\mathbf{i}}, \tag{50}$$

where $C_{\mathbf{j},\mathbf{i}}$ are coefficients. In the present work, $C_{\mathbf{j},\mathbf{i}}$ are obtained following the algorithm proposed in [51]. Then the nodal sensitivity of $\mathbf{p}_{\mathbf{j}}$ reads

$$\frac{\partial \mathbf{p}_{\mathbf{j}}}{\partial \alpha_s} = C_{\mathbf{j},\mathbf{i}} \frac{\partial \widetilde{\mathbf{p}}_{\mathbf{i}}}{\partial \alpha_s}. \tag{51}$$

6.3 Sensitivity propagation from domain boundary to the coarse mesh

During the mesh generation process, we extract Bézier segments from B-splines through knots insertion. As shown in Fig. 14, as the B-splines control points $\mathbf{c}_1$ changes, the control points of Bézier triangles on the design boundary, $\widetilde{\mathbf{p}}^B$, change accordingly. The internal control points of the coarse mesh, $\widetilde{\mathbf{p}}^I$, are then updated during the optimization by solving the pseudo linear elasticity problem Eq. (18).

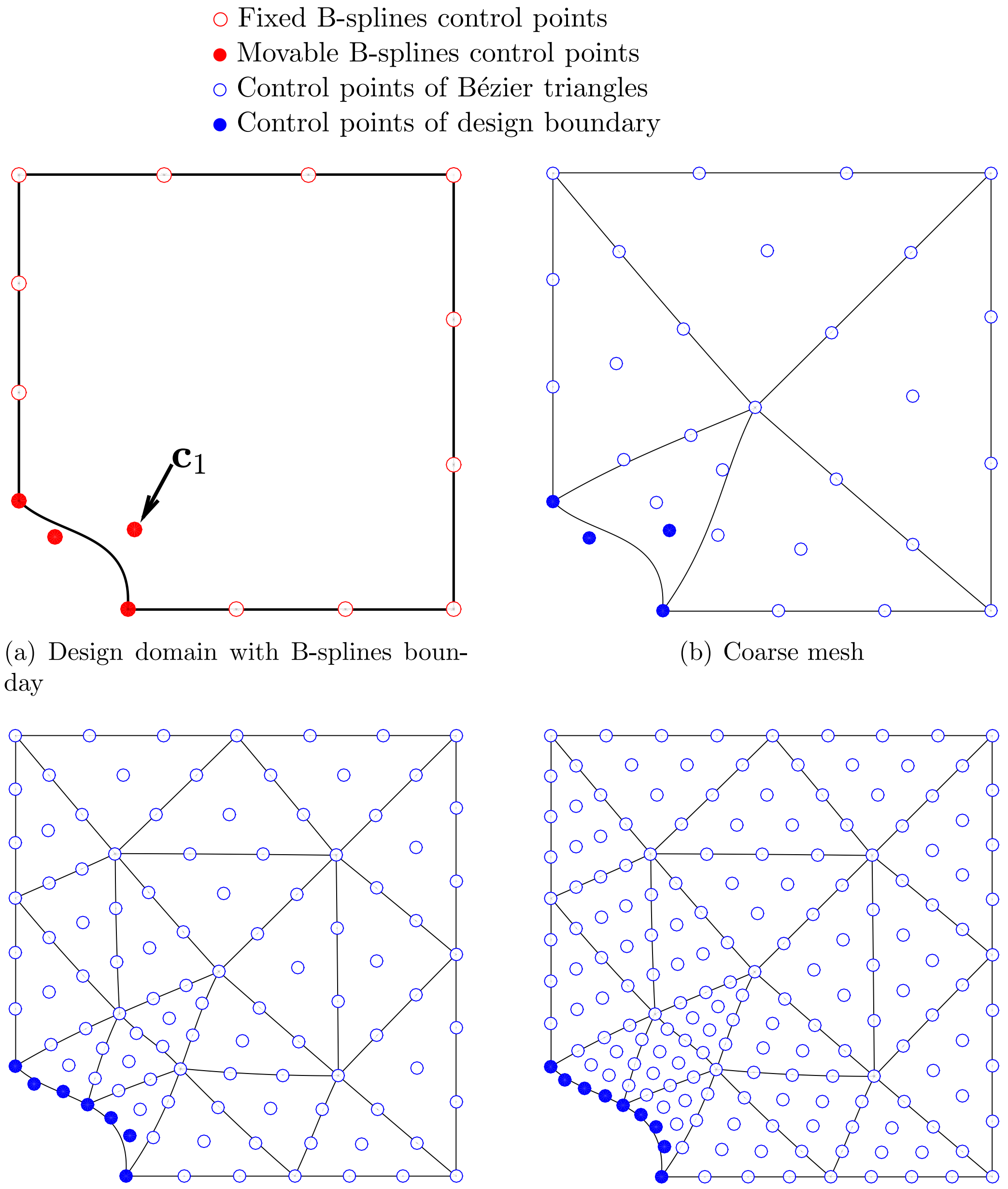
○ Fixed B-splines control points
● Movable B-splines control points
○ Control points of Bézier triangles
● Control points of design boundary
$\mathbf{c}_1$

(a) Design domain with B-splines boun-day

(b) Coarse mesh

(c) Fine mesh with refinement

(d) Fine mesh with refinement and degree elevation

Figure 14: Nodal sensitivity propagation from B-splines boundary to the fine Bézier triangular mesh. Control point $\mathbf{c}_1$ moves from the initial position as shown in 2(a) to the current position.

Knots insertion For a given B-spline curve with control points $\mathbf{c}_0, \mathbf{c}_1, \cdots, \mathbf{c}_n$ and knot vector $\{\mu_0, \mu_1, \cdots, \mu_{n+d+1}\}$, a new knot value $\bar{\mu}$ can be inserted into the knot vector without change the shape of the B-spline curve as follows.

Step 1 Find the knot span $[\mu_l \ \mu_{l+1}]$ containing $\bar{\mu}$

Step 2 Find the associated control points $\mathbf{c}_{l-d}, \mathbf{c}_{l-d+1}, \cdots, \mathbf{c}_l$

Step 3 Calculate d new control points

$$\mathbf{d}_i = (1 - \beta_i)c_{i-1} + \beta_i c_i, \tag{52}$$

with

$$\beta_i = \frac{\bar{\mu} - \mu_i}{\mu_{i+d} - \mu_i}, \quad l - d + 1 \le i \le l.$$

Then we have the new knot vector $\{\mu_0, \mu_1, \cdots, \mu_l, \bar{\mu}, \mu_{l+1}, \cdots, \mu_{n+d+1}\}$ and new control points $\{\mathbf{c}_0, \mathbf{c}_1, \cdots, \mathbf{c}_{l-d}, \mathbf{d}_{l-d+1}, \mathbf{d}_{l-d+1}, \cdots, \mathbf{d}_l, \mathbf{c}_l, \mathbf{c}_{l+1}, \cdots, \mathbf{c}_n\}$.

To extract the Bézier segements, the above procedures are repeated until each knot of the B-spline curve has multiplicity d. Finally, the control points of Bézier curves are linear combination of those of B-spline curve and we have

$$\widetilde{\mathbf{p}}_j^B = \sum_i M_{ji}\mathbf{c}_i. \tag{53}$$

Then the nodal sensitivities of the Bézier control points on the boundary read

$$\frac{\partial \widetilde{\mathbf{p}}_j^B}{\partial \alpha_s} = M_{ji}\frac{\partial \mathbf{c}_i}{\partial \alpha_s}. \tag{54}$$

Mesh movement by solving linear elasticity equation The variation of the internal control points of the coarse mesh is determined by solving the pseudo linear elasticity problem Eq. (18). From Eq. (19), we have

$$\frac{\partial \widetilde{\mathbf{p}}^I}{\partial \alpha_s} = \mathbf{A}\frac{\partial \widetilde{\mathbf{p}}^B}{\partial \alpha_s}. \tag{55}$$

7 Numerical examples

In this section, numerical examples are presented to show the validity of the proposed isogeometric shape optimization framework. All examples assume the plane stress conditions and use the same plate thickness $t_e = 1.0$. The convergence criteria used in our optimization algorithm is the change of the objective function value

$$e =\mid \frac{\mathcal{C}^k - \mathcal{C}_{k-1}}{\mathcal{C}_0} \mid,$$

where $\mathcal{C}^k$ represents the structural compliance at the k-th iteration. Unless otherwise specified, e is set to 1e-6 in our work. The gradient-based optimization algorithm, MMA[52], is utilized to conduct the optimization. The sensitivities of the objective function and constraints are validated by the finite difference method.

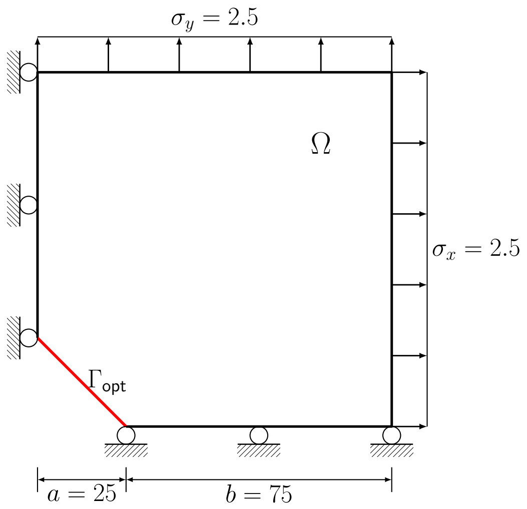

Figure 15: The design model of a plate with a hole.

Table 1: Comparison of analytical sensitivity with finite differencing

α	$\frac{\Delta\mathcal{C}}{\Delta\alpha}$	$\frac{\partial\mathcal{C}}{\partial\alpha}$	$\frac{\partial\mathcal{C}/\partial\alpha}{\Delta\mathcal{C}/\Delta\alpha}$	$\frac{\Delta V}{\Delta\alpha}$	$\frac{\partial V}{\partial\alpha}$	$\frac{\partial V/\partial\alpha}{\Delta V/\Delta\alpha}$
1	0.17246	0.17245	99.9949	-6.25000	-6.25000	100.0000
2	0.02189	0.02189	99.9955	-6.25000	-6.25000	100.0000
3	0.02279	0.02279	99.9928	-6.25000	-6.25000	100.0000

7.1 A plate with a hole

The benchmark problem, a plate with a hole, is first studied. The Young's modulus is 210 and the Poisson's ratio is 0.3. The maximum volume constraint for the problem is 9600. For this example, the move limits of α are set to $\alpha_x \in [0, 30], \alpha_y \in [0, 30]$, so that the optimal hole profile can be found. The design model, including boundary conditions, loads, and design boundary, is shown in Fig. 15. We use five cubic B-splines curves to represent the design domain and the control points for design boundary are indicated as red solid circle (Figure 16(a)). For this simple problem, only five Bézier triangles are used for the coarse mesh (see Fig. 16(b)). For the coarse mesh, we select the mesh size as 100 during the mesh generation process. As cubic Bézier triangles are used in coarse mesh, the control points on the design boundary are same with the control points of the B-splines. Figure 16(d) shows the initial fine mesh used for isogeometric analysis, which is generated by refining the coarse mesh in Fig. 16(b) three times.

Before optimization, the analytical sensitivity is checked by finite differencing, as shown in Table 1. $\Delta/\Delta\alpha$ and $\partial/\partial\alpha$ represent the finite difference and the analytical sensitivities, respectively. $\Delta\alpha$ represents the perturbation amount of optimization variables and it is set to 0.001. The sensitivities of the compliance $\mathcal{C}$ and the volume V are checked. It can be observed from Table 1 that the analytical sensitivities excellently agree with the finite difference sensitivities. The computing cost for the sensitivity analysis is seen to be inexpensive. This example is performed on a HP EliteDesk 800 G1 desktop with an Intel(R) i7-4790 processor, 16GB memory, Windows 7 SP1, and MATLAB R2014b. The fine mesh (Figure 16(c)) for analysis has 320 elements and 3002 degrees of freedom

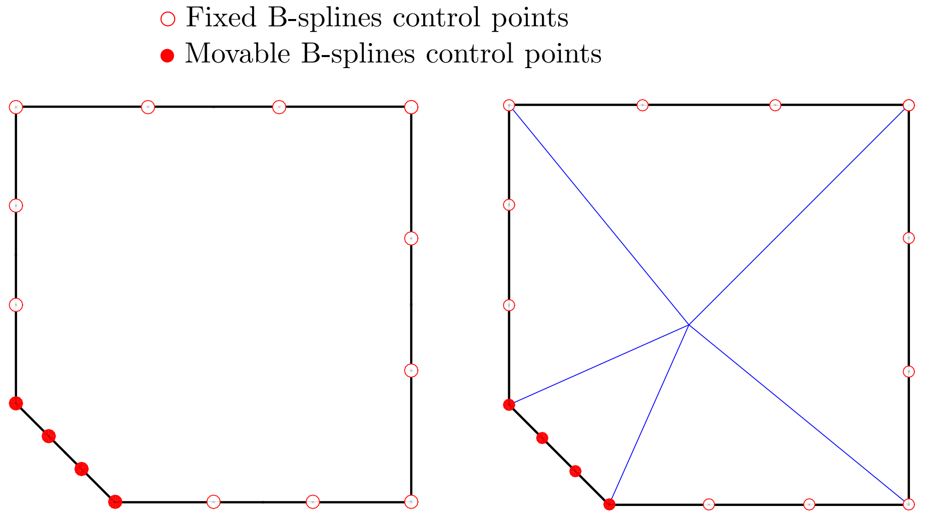
○ Fixed B-splines control points
● Movable B-splines control points

(a) Design domain with B-splines bounday

(b) Initial coarse cubic Bézier triangular mesh

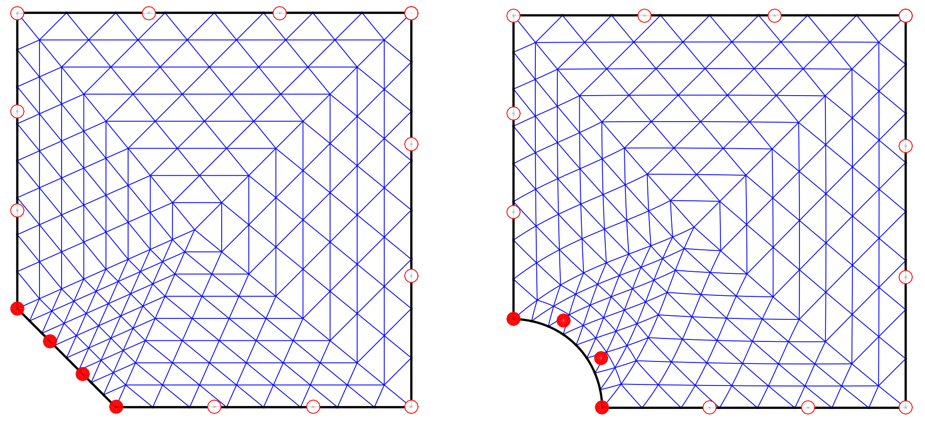

(c) Initial fine cubic Bézier triangular mesh

(d) Optimized result

Figure 16: The design of a plate with a hole.

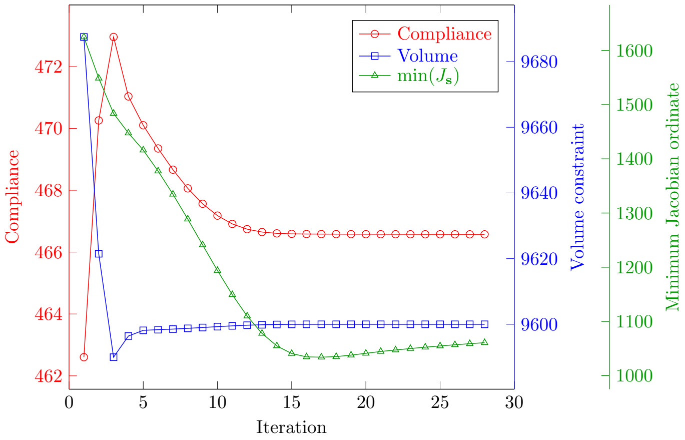

Figure 17: The convergence history for the design of a plate with a hole.

(DOFs). The CPU cost is 2.5 seconds for the isogeometric analysis and 1.8 seconds for the sensitivity analysis. As the coarse mesh (Figure 16(b)) only has 5 elements and 62 DOFs, it only takes 0.0065 seconds for solving the pseudo linear elasticity problem for mesh movement. This verifies that the computational cost for mesh movement can be significantly saved based on the coarse mesh. For comparison, we test the plate hole problem in [11], which is based on NURBS representation, and it has 2312 DOFs. It takes 2.8 seconds for the isogeometric analysis and 2 seconds for the sensitivity analysis. It is seen that, even though the proposed method needs to solve a pseudo linear elasticity problem for mesh movement, the total computational cost is still comparable to the cost of the NURBS-based shape optimization.

The compliance of the problem converges to 466.5719 after 28 iterations and the optimized shape is shown in Fig. 16(d). The convergence history of the compliance, volume constraint and minimum Jacobian ordinate, is shown in Fig. 17. We can see that the minimum Jacobian ordinate is always positive as the design boundary doesn't change too much. In this case, mesh optimization and regeneration are not needed.

For an infinite plate, the theoretical profile of the hole for this example should be an exact circle under equal biaxial loading. Here, how well our results match the analytical solution is investigated. Then, we redo the optimization by pre-setting weights of the variable control points which allow the exact representation of the expected circle. The specified weights are $\{1, \frac{1+\sqrt{2}}{3}, \frac{1+\sqrt{2}}{3}, 1\}$. The two optimized profiles with the specified and unit weights are shown in Fig. 18(a). For comparison, the exact circular arc is also plotted in Fig. 18(a). The differences among the three profiles are visually indistinguishable. Figure 18(b) plots the magnified view of the profiles. We can observe that even though the control points of the three curves are different, the hole profiles remain almost the same. For better observing the differences among these three profiles, the radial distances from the three profiles to the circle center are shown in Fig. 19. The maximum deviation from the theoretical circle center is 0.234% percent for the B-spline representation and 0.231% for the NURBS representation. Compared to the results in [11], the difference between the B-splines and NURBS representations is relatively small in our work. In summary, as the differences among the three profiles are so small compared with results from [9, 11], we can come to the conclusion that our method obtains the right solution.

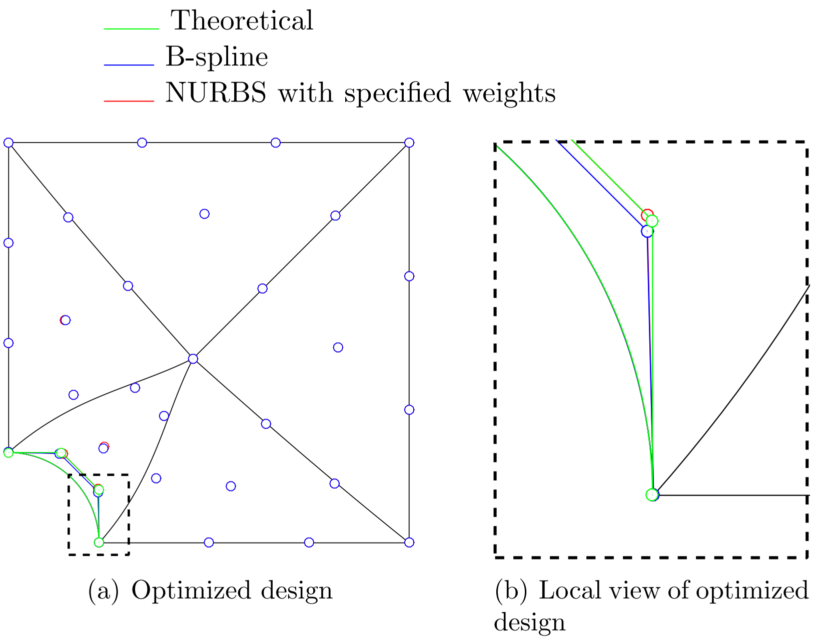

(a) Optimized design

(b) Local view of optimized design

Figure 18: Comparison of optimized hole profiles for different boundary representations.

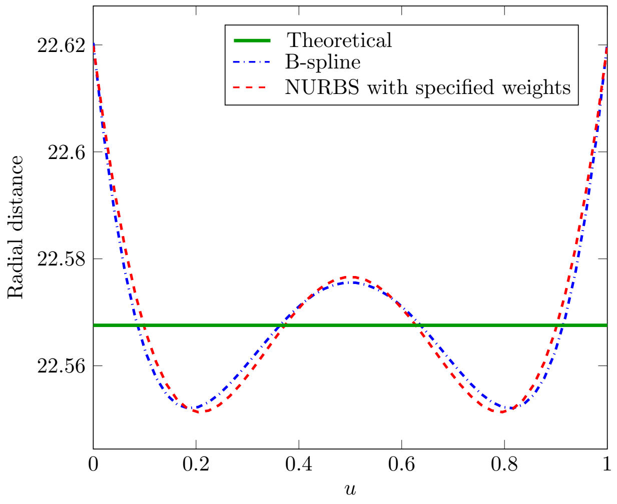

Figure 19: Radial distance from the optimized hole profiles to the circle center.

7.2 A cantilever with holes

We first study a cantilever beam with one hole, which is drawn from [53]. The dimensions, loads and design boundaries are shown in Fig. 20(a). The Young's modulus is 15 and the Poisson's ratio is 0.35. The maximum volume constraint for the problem is 95. The domain boundary is defined with quadratic B-splines. For this problem, the move limits of α are set to $\alpha_x \in [0, 20], \alpha_y \in [-20, 20]$. As shown in Fig. 20(c), quadratic Bézier triangles are used for the coarse mesh. During the mesh generation process, the mesh size is set to 0.8 in the example. The fine mesh is generated by once degree elevation and once uniform refinement. Since the thickness of connections are relatively large compared with the mesh size in the example, the local refinement and the distance control are unnecessary.

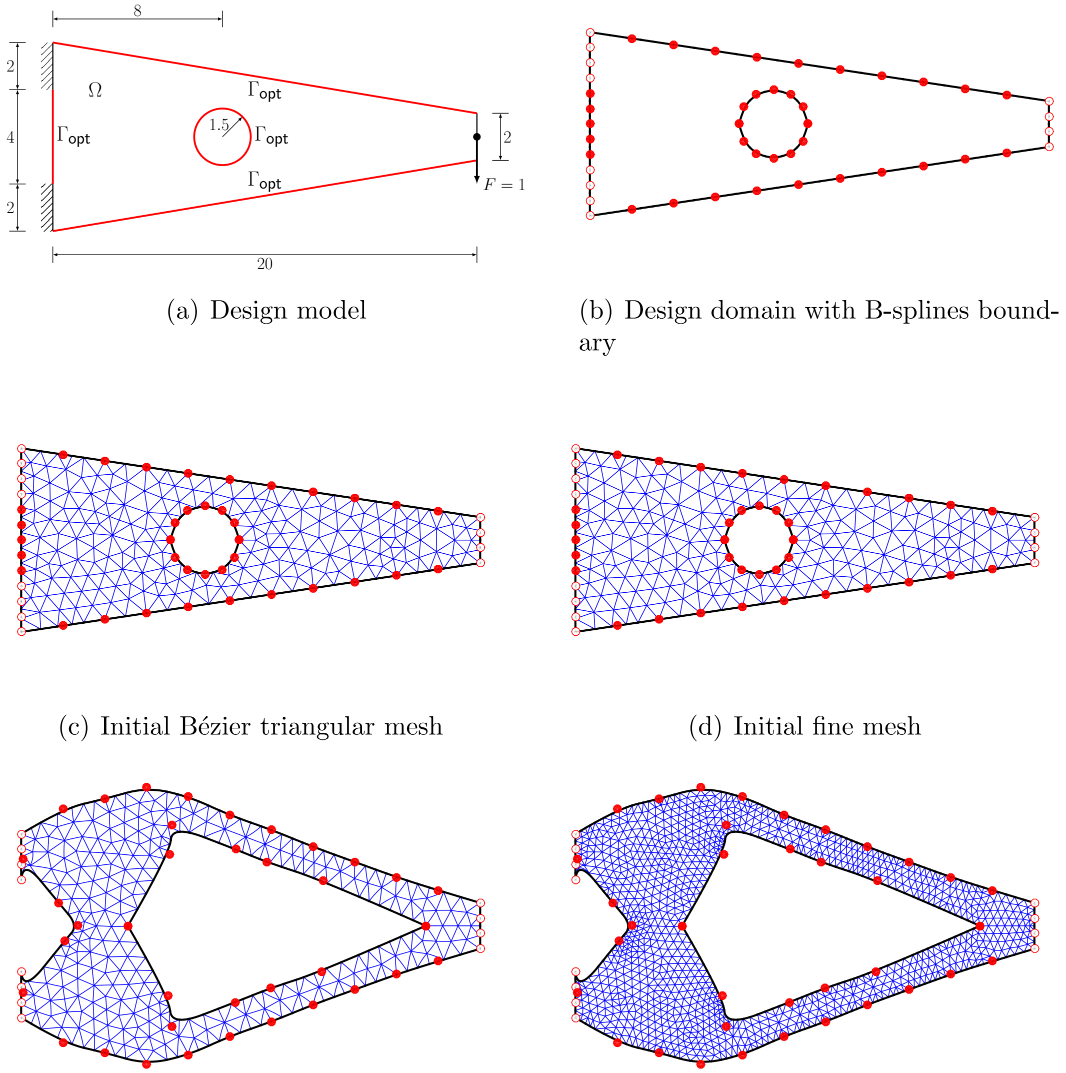

(a) Design model

(b) Design domain with B-splines boundary

(c) Initial Bézier triangular mesh

(d) Initial fine mesh

(e) Optimized coarse mesh

(f) Optimized fine mesh

Figure 20: Design of a cantilever with one hole.

The optimal result is shown in Fig. 20(f), with the compliance of 19.57 and the volume of 94.99. The optimized shape in Fig. 20(f) is similar with the result in [53]. Figure 21 shows the convergence history of the compliance, the volume constraint and the minimum

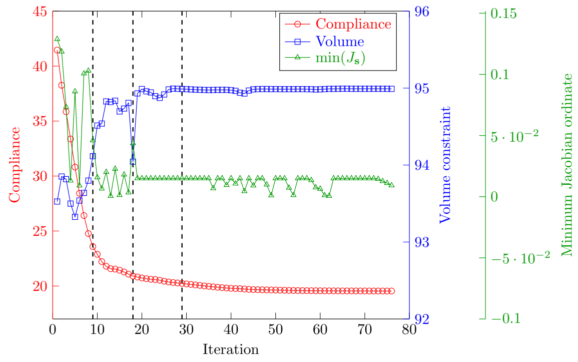

Figure 21: Convergence history for the design of a cantilever with one hole. Dashed lines show the iterations at which remeshing is invoked.

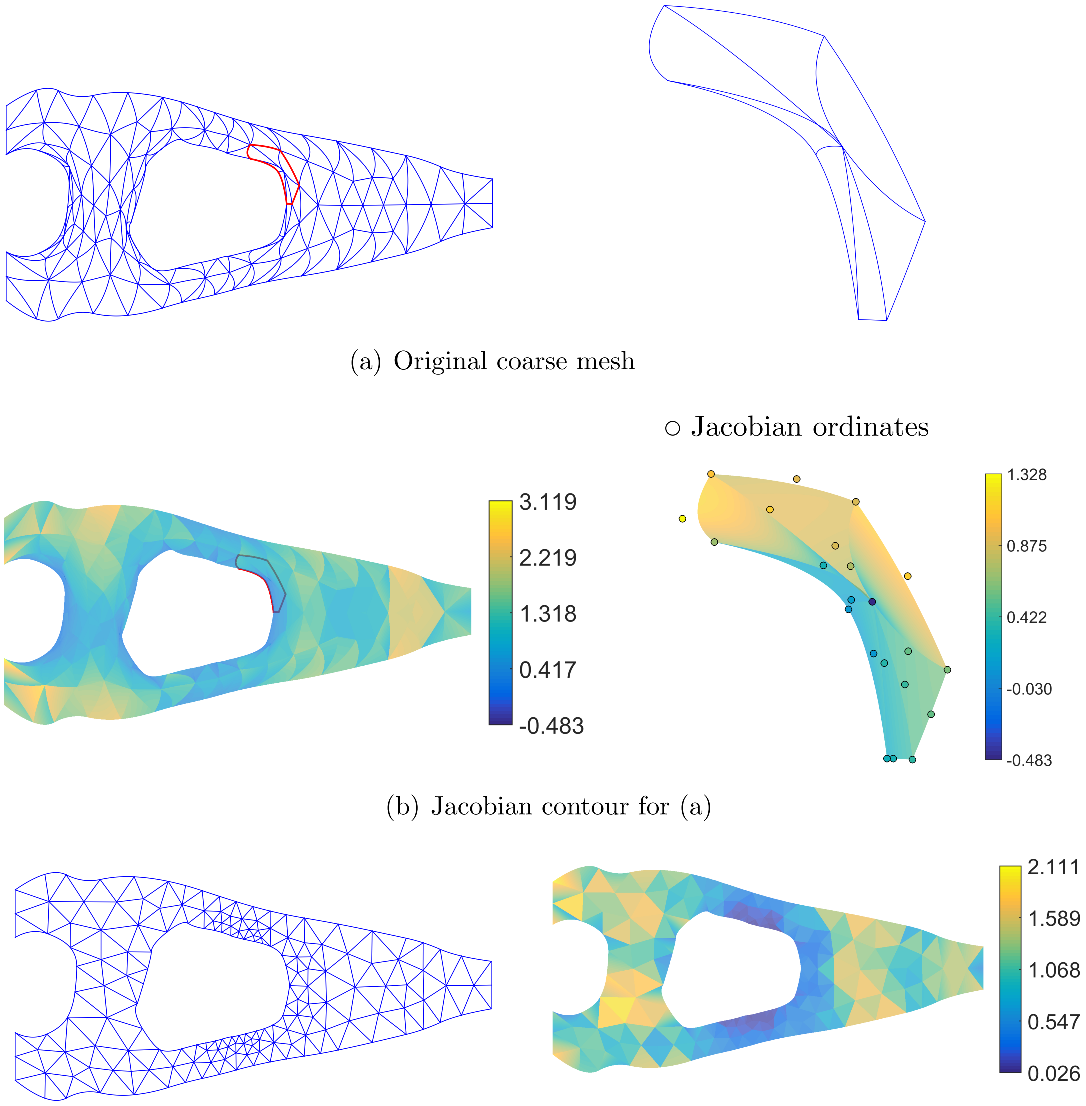

(a) Original coarse mesh

(b) Jacobian contour for (a)

(c) Regenerated valid mesh

(d) Jacobian contour for (c)

Figure 22: Cantilever with one hole: remeshing at the 12th iteration to avoid mesh-folding.

Table 2: Summary of the optimization results for the cantilever beam

Type	1 hole	3 holes	6 holes	9 holes
Compliance	19.57	17.52	17.24	17.16

Jacobian. It can be easily seen that the minimum Jacobian ordinate is larger than zero during the optimization, which means the mesh is valid. The dashed lines in Fig. 21 show the iterations at which we do remeshing. For this example, we only remesh three times at the 9th, 18th and 29th iterations. Therefore, the remeshing process will not increase computational cost too much as only a few remeshing operations are needed. We can observe that the change of the compliance and volume constraint are very small after remeshing. This is because the boundary control points, i.e. optimization variables, remain the same during the remeshing process.

During the optimization process, the mesh can be largely distorted due to the large deformation of design boundary. Figure 22(a) shows the coarse mesh at the 9-th iteration before. We can see that the triangles around the hole are largely distorted and self-intersections appear. In Fig. 22(b), the corresponding Jacobian contour and ordinates are plotted. From the locally magnified inset figure, it is clear that the negative Jacobian ordinate locates in the triangle where self-intersection happens. In order to avoid large distortions and self-intersections, the mesh is regenerated based on the same domain boundary. The regenerated coarse mesh is shown in Fig. 22(c) and the corresponding Jacobian contour and ordinates are shown in Fig. 22(d), respectively. The new mesh uses more triangular elements around the hole and the elements aren't largely distorted. The minimum Jacobian ordinate also becomes positive, with the value of 0.026.

In order to show that our method can work well for design problems with complex geometry and allow large deformation of the design boundary, we increase the number of holes in the design domain. The similar problems are also studied in [53]. Except adding the number of holes, other dimensions and loading conditions are same with those in the previous example. The maximum volume constraint is still 95. The Young's modulus is 15 and the Poisson's ratio is 0.35. The domain boundary is defined with quadratic B-splines. For the mesh generation process in this example, the mesh size is selected as 0.8. In order to avoid the single elements at the thin connections between holes, we do local refinement for each generated coarse mesh. The coarse mesh uses quadratic Bézier triangles. The fine mesh is obtained through once degree elevation and once uniform refinement. Therefore, for the fine mesh, at least four layers of elements are guaranteed within the thin connections. To prevent intersections of holes, the distance constraint checking strategy is applied. The prescribed minimum squared distance, $D_{\min}$, is 0.04, i.e. the distance between two curves should be larger than 0.2. The small limit is selected so that the optimum design can be found.

The optimized designs for three, six and nine holes are shown in Figs. 23, 24 and 25, respectively. Table 2 lists the resulting compliance for the cantilever with different number of holes. We can observe that as the optimal compliance decreases with the number of holes. This is because more holes allow for larger design space to search the optimal design. It can also be observed that this advantage becomes small starting from three holes.

We use the nine holes example to illustrate the local refinement process and show the distance control. The regenerated coarse mesh at the 95th iteration is shown in Fig. 26(a). We can observe that only one layer of elements exist within the thin connections

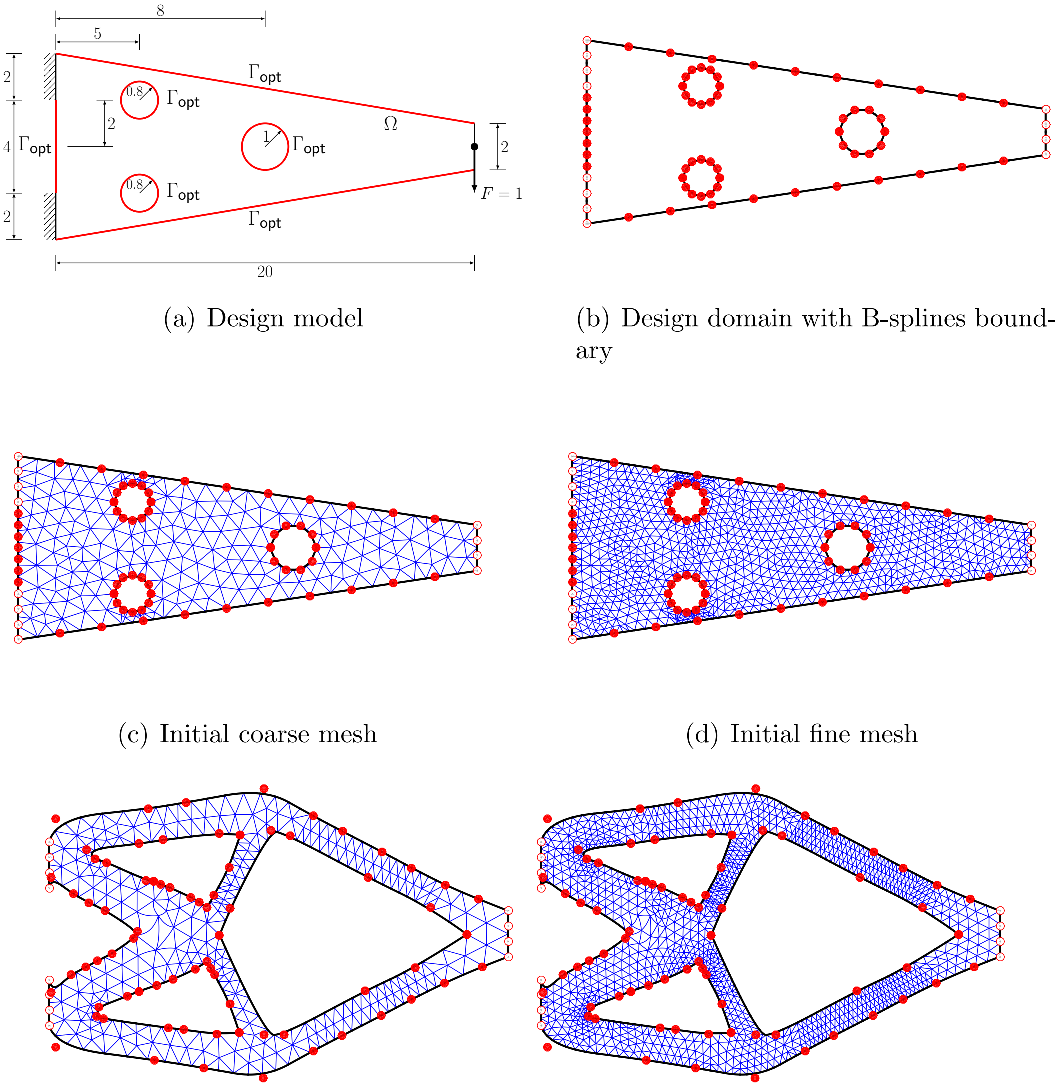

(a) Design model

(b) Design domain with B-splines boundary

(c) Initial coarse mesh

(d) Initial fine mesh

(e) Optimized coarse mesh

(f) Optimized fine mesh

Figure 23: Design of a cantilever with three holes.

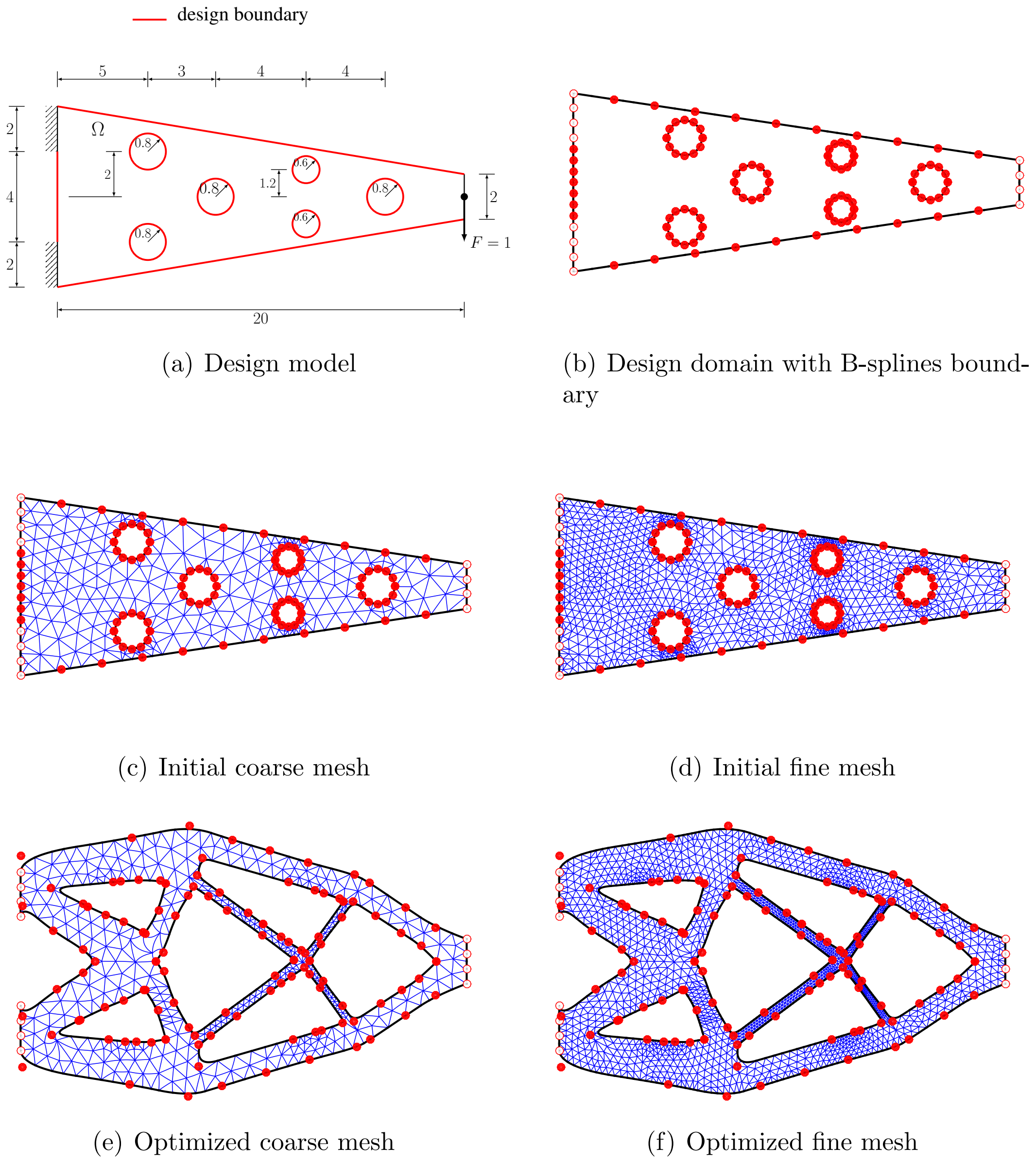

(a) Design model

(b) Design domain with B-splines boundary

(c) Initial coarse mesh

(d) Initial fine mesh

(e) Optimized coarse mesh

(f) Optimized fine mesh

Figure 24: Design of a cantilever with six holes.

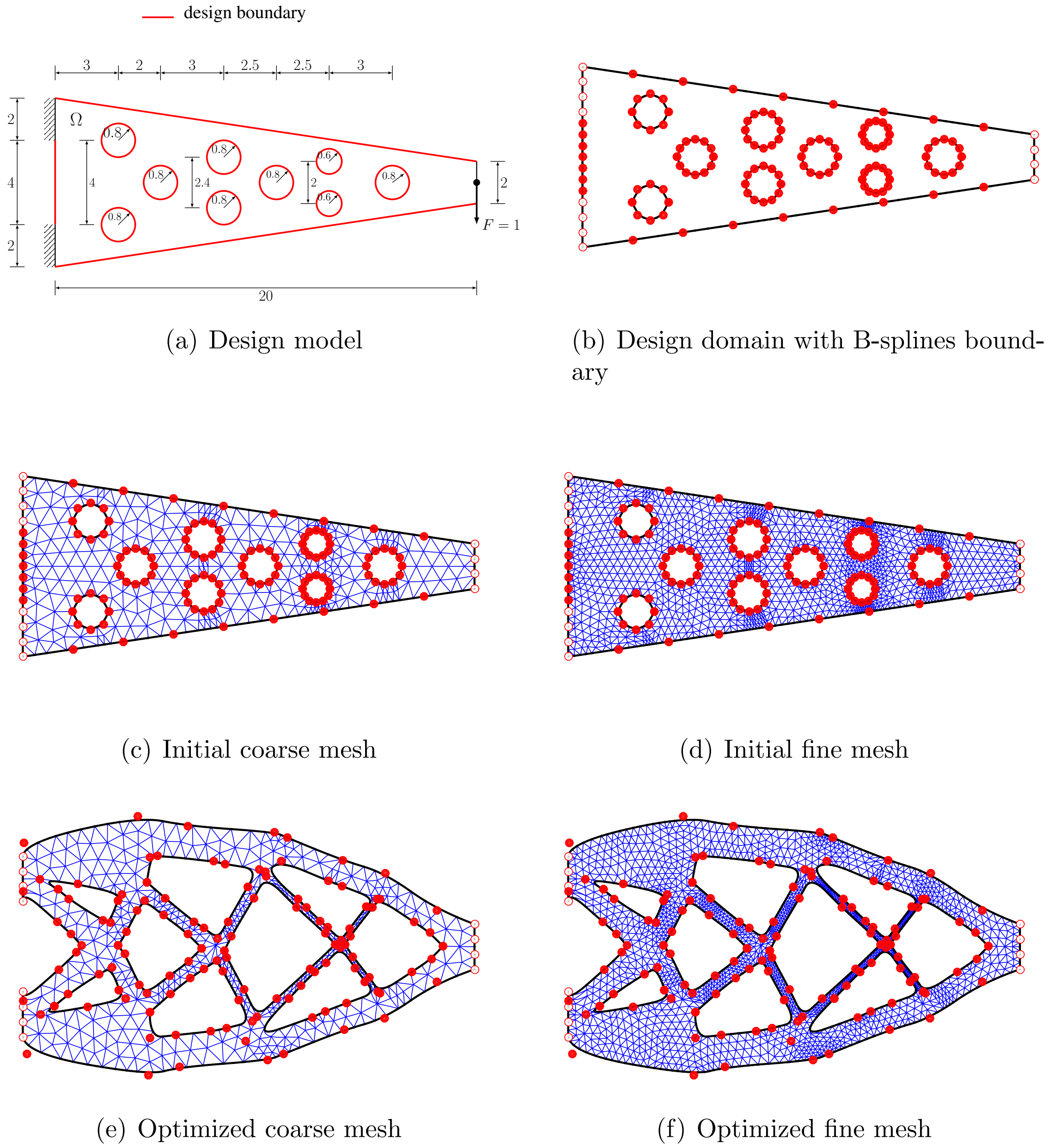

(a) Design model

(b) Design domain with B-splines boundary

(c) Initial coarse mesh

(d) Initial fine mesh

(e) Optimized coarse mesh

(f) Optimized fine mesh

Figure 25: Design of a cantilever with nine holes.

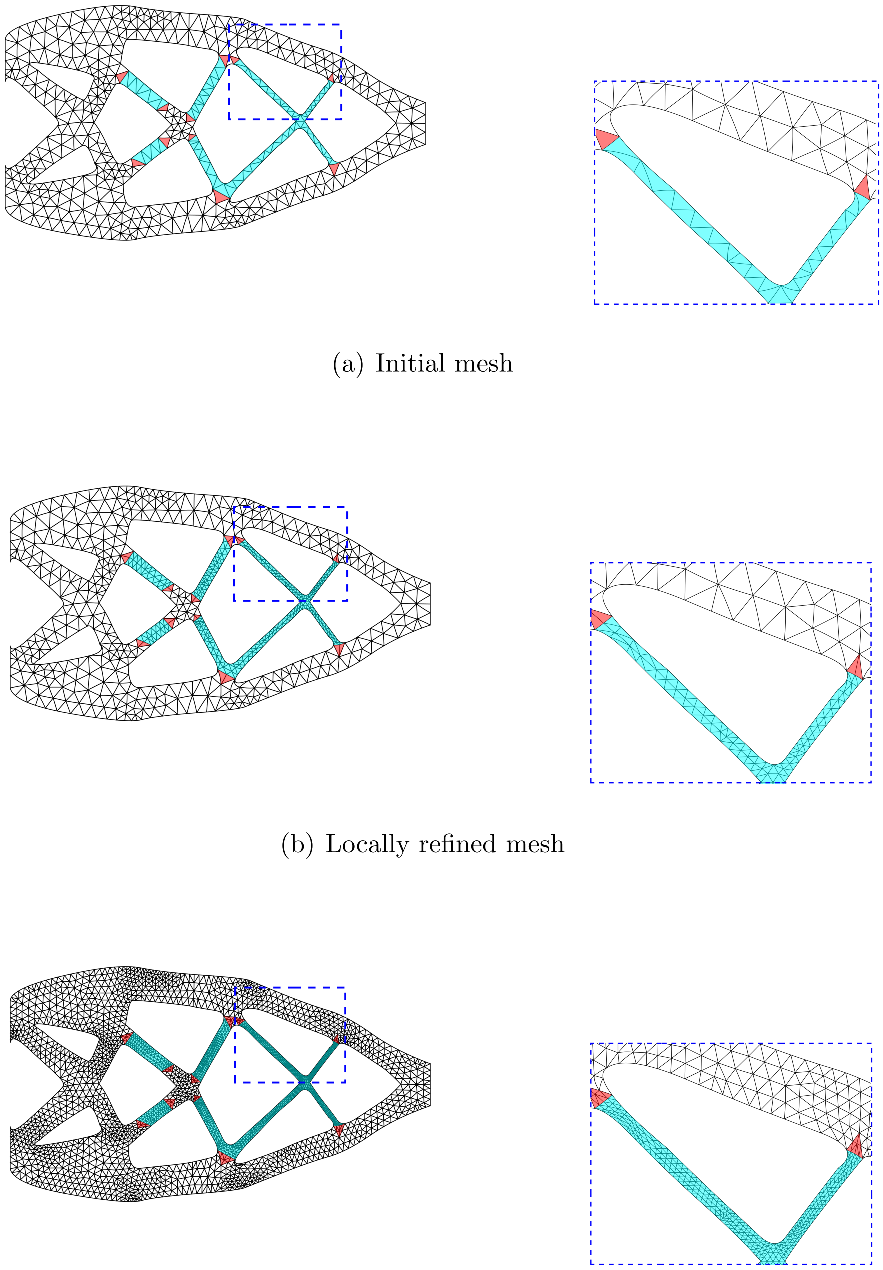

(a) Initial mesh

(b) Locally refined mesh

(c) Uniformly refined mesh

Figure 26: Cantilever with nine holes: local and uniform refinement of single-element thin connections. After refinements, at least four layers of triangles exist at the thin connections.

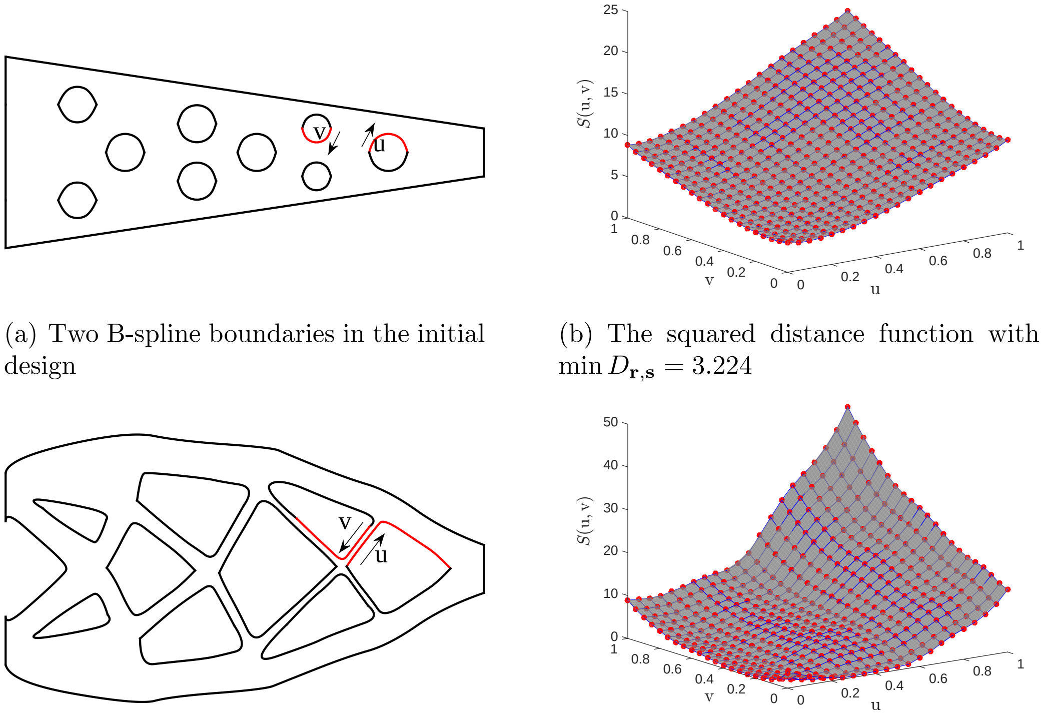

(a) Two B-spline boundaries in the initial design

(b) The squared distance function with $\min D_{\mathbf{r},\mathbf{s}} = 3.224$

(c) Two B-spline boundaries in the final design

(d) The squared distance function with $\min D_{\mathbf{r},\mathbf{s}} = 0.041$

Figure 27: Cantilever with nine holes: the squared distance visualization between two boundaries in the initial and final designs, respectively.

between holes. Figure 26(b) shows the locally refined mesh, in which the single elements between holes are subdivided. After local refinement, at least two layers elements are guaranteed in the thin connections for the coarse mesh. For the fine mesh, once uniform refinement is further applied to the coarse mesh. We can observe from Fig. 26(c) that at least four layers of elements exist within the thin connections for the fine mesh.

For the distance control, we visualize the squared distance function between two B-spline boundaries. Figure 27(a) and (c) show two B-spline boundaries in the initial and final designs (Figure 25(c) and (d)), respectively. The squared distance function between these two boundaries are shown in Fig. 27(b) and (d). Red points are the squared distance ordinates. The minimum ordinates between these two boundaries are 3.224 for the initial design and 0.043 for the final design. That is, the distance constraints are active in the final design. For the two B-spline boundaries, we first extract Bézier segments and then derive the squared distance ordinates between each pair of Bézier segments separately on two boundaries. We can observe from Fig. 27(b) and (d) that the convex hull of the squared distance function is very compact. Based on this fact, if the distance constraints are active, the discrepancy between the real distance between B-spline boundaries and the prescribed limit will be very small.

7.3 Auxetic materials design

In this subsection, two examples are presented for NPR materials design. The first example considers a unit cell that is widely studied in literatures, e.g. [54, 30, 50]. This unit cell has simple geometry and good manufacturability. In the second example, a relatively complex unit cell is optimized to show the ability of the proposed shape optimization approach for complex topology. The geometry of the unit cell is motivated by the topological design in [55]. In both examples, the optimized unit cells are periodically arranged to form cellular structures. These periodic cellular structures are represented by the B-splines boundaries, which can be easily linked to CAD systems. Further, Bézier triangular meshes are generated for these periodic cellular structures and numerical tests are conducted to verify the NPR behavior.

7.3.1 Unit cell with simple geometry

The first example optimizes a unit cell with a target Poisson's ratio $\nu = -1$. The target elastic properties are prescribed as $C^\star_{1111} = 0.1$, $C^\star_{2222} = 0.1$ and $C^\star_{1122} = -0.1$. The corresponding weights in the objective function are set as $\omega_{1111} = 0.5$, $\omega_{2222} = 0.5$ and $\omega_{1122} = 5$, which are selected based on the suggestions in [50]. The Young's modulus of the solid material is 0.91 and the Poisson's ratio is 0.3. The given volume fraction of the unit cell is 0.25. The unit cell is represented by quadratic B-splines boundaries. The dimension of a quarter of the unit cell is 50 by 50. The move limits of B-splines control points, α, are set to $\alpha_x \in [0, 50], \alpha_y \in [0, 50]$, so that every control point can move around freely in the unit cell. The design domain is discretized by quadratic Bézier triangles. The fine mesh is generated by uniformly refining the coarse mesh. In the fine mesh, at least four layers elements are guaranteed within the thin connections.

Figure 28 (a) and (b) show the initial coarse mesh and fine mesh of the 1/4 unit cell, respectively. The optimized coarse mesh and fine mesh are shown in Fig. 28 (c) and (d). The effective elastic tensor C^H for the optimized design is

$$C^H = \begin{bmatrix} 0.0577 & -0.0433 & 0 \\ -0.0433 & 0.0578 & 0 \\ 0 & 0 & 0.0012 \end{bmatrix},$$

which corresponds a negative Poisson's ratio $\nu = C^H_{1122}/C^H_{1111} = -0.75$. In our implementation, as we use the same weights ω_{1111} and ω_{2222}, the designed unit cell should have the same value for C^H_{1111} and C^H_{2222}. However, due to asymmetric meshes during the optimization, the optimized design can be asymmetric. Hence, there is a small difference between ν_{12} and ν_{21}, i.e. $\nu_{12} = 0.7491$ and $\nu_{21} = 0.7504$. The difference between the optimized and desired negative Poisson's ratio partly results form the limitations of volume constraint and symmetric boundary conditions. The convergence history of the example is shown in Fig. 29. The optimization algorithm gets converged in 32 iterations and re-meshing is invoked at the 20th iteration.

The unit cell is shown in Fig. 30(a), which is geometrically similar with the design by topology optimization [50]. The unit cell is periodically repeated to generate the cellular structure in Fig. 30(b). As this periodic cellular structure is also represented by B-splines boundaries, it can be easily integrated to CAD systems for manufacturing.

To numerically verify the NPR behavior, Bézier triangular mesh is also generated for the periodic cellular structure in Fig. 30(b). The dimension of the cellular structure is 400 by 400. The boundary condition of the numerical test is shown in Fig. 31(a). Left and bottom boundaries are supported and a displacement with a magnitude of -40 is applied on the right boundary. The initial shape and deformed shape of the cellular structure are shown in Fig. 31(b) and (c), respectively. The color contour in Fig. 31(c) shows the displacement in Y direction. As shown in Fig. 31(c), the structure shrinks

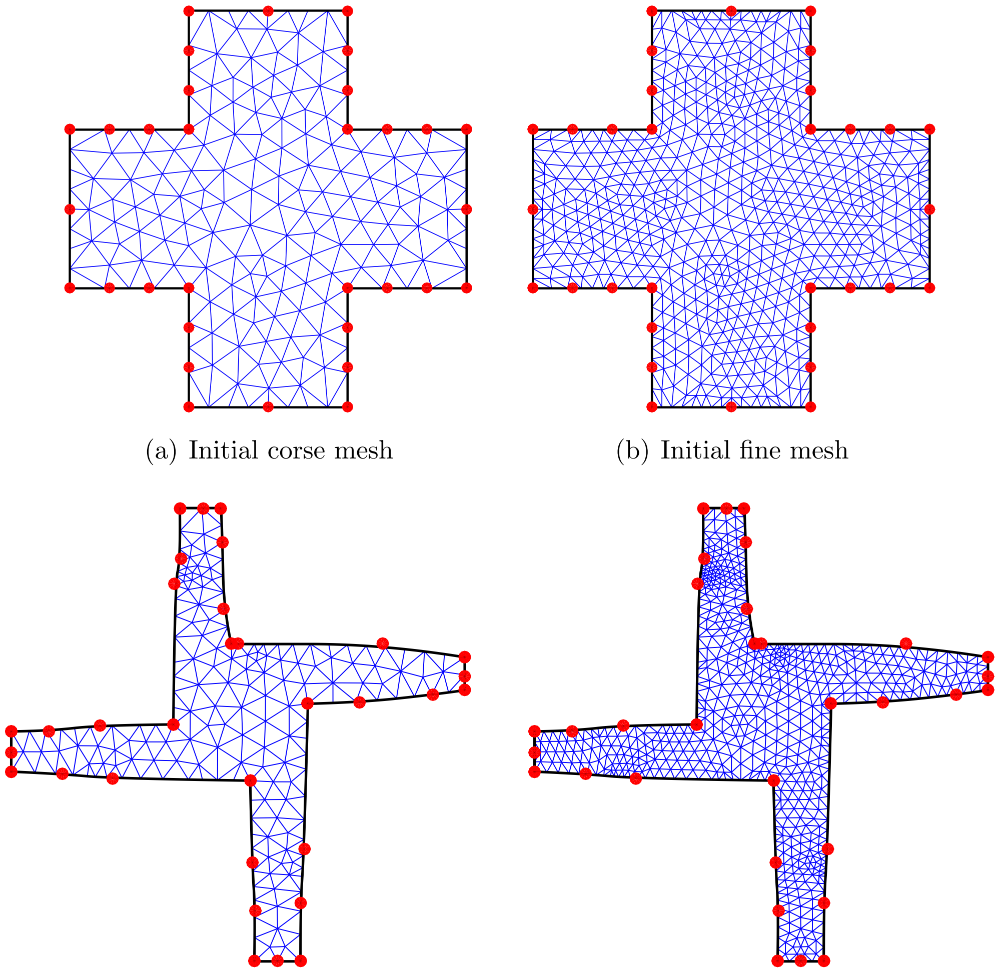

(a) Initial corse mesh

(b) Initial fine mesh

(c) Optimized corse mesh

(d) Optimized fine mesh

Figure 28: Design of a quarter of the unite cell with simple geometry.

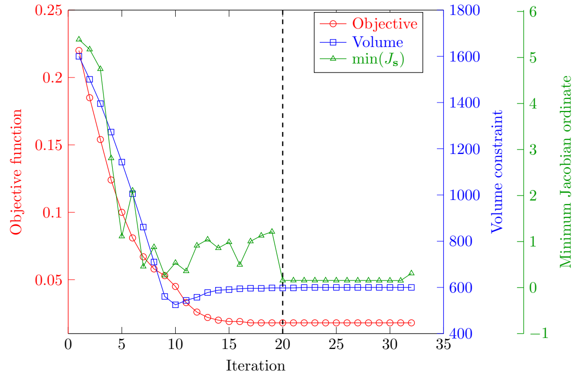

Figure 29: Convergence history for the design of the unit cell with simple geometry. Dashed lines show the iterations at which remeshing is invoked.

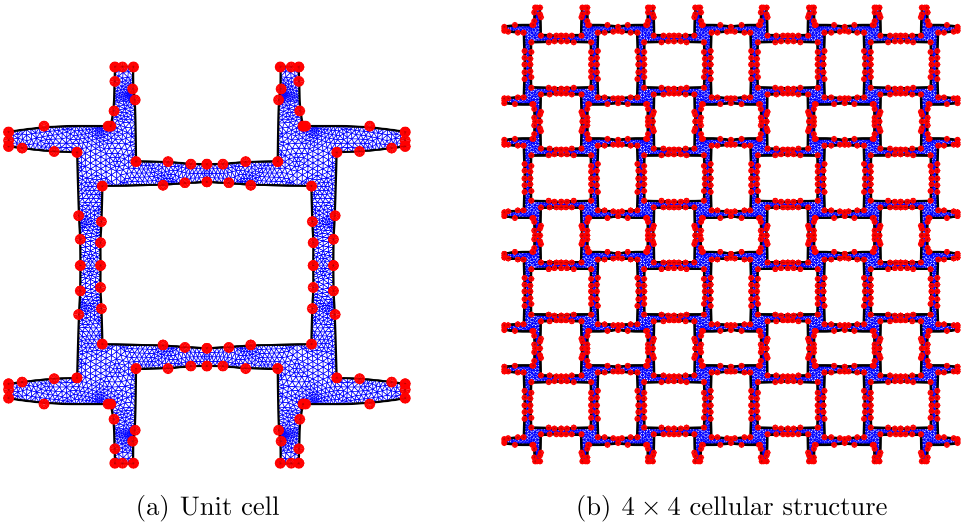

Figure 30: Unit cell and the periodically arranged cellular structure.

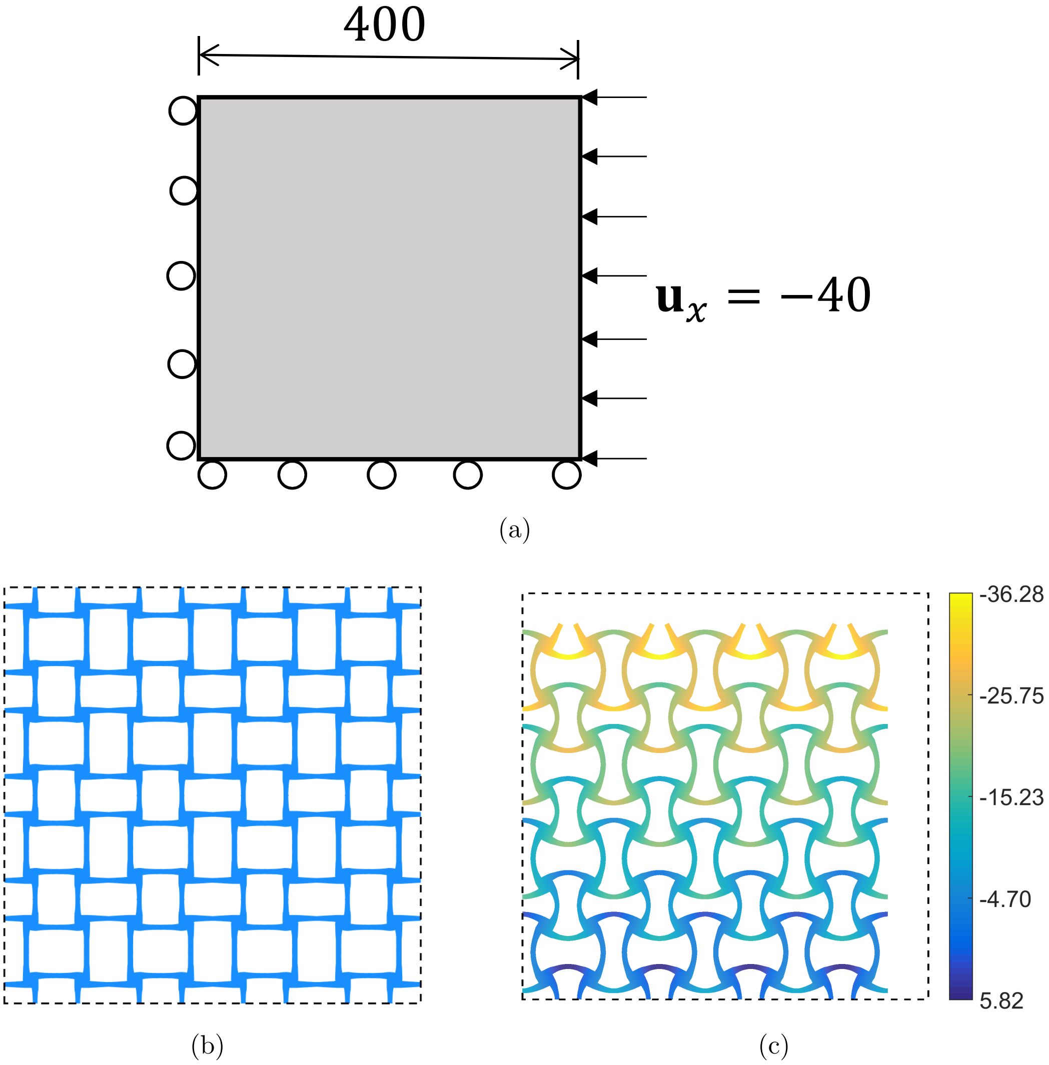

Figure 31: Numerical verification of the NPR behavior. (a) Boundary conditions. (b) Initial shape. (c) Deformed shape.

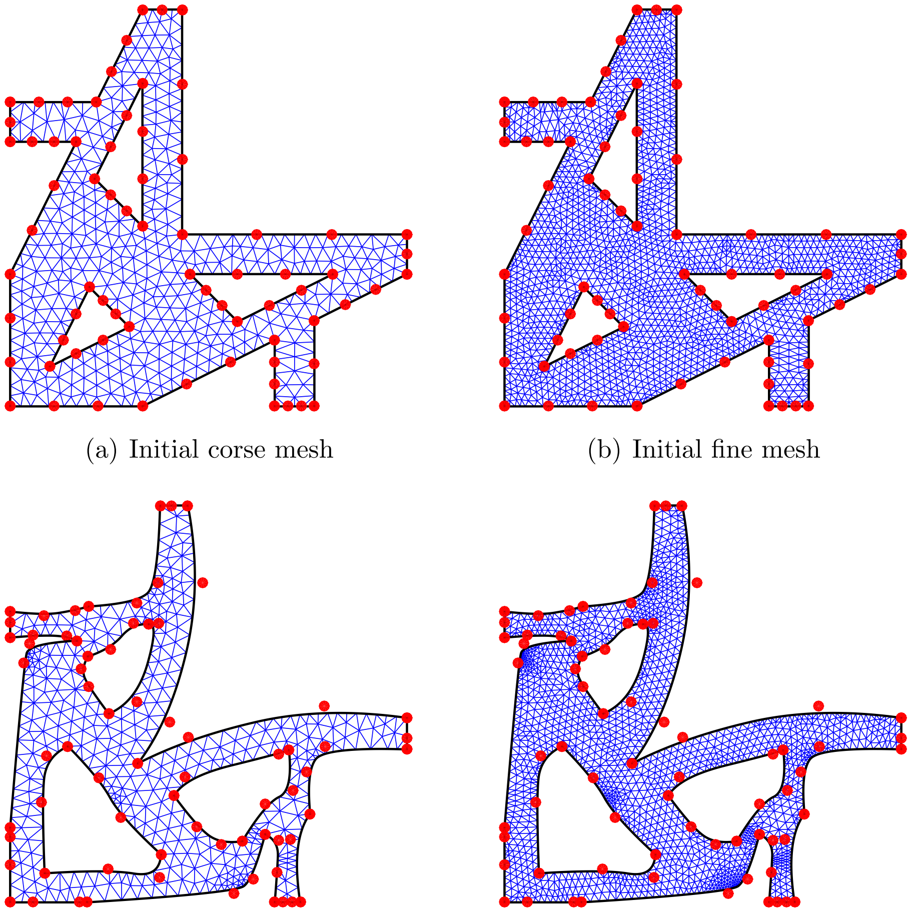

(a) Initial corse mesh (b) Initial fine mesh

(c) Optimized corse mesh (d) Optimized fine mesh

Figure 32: Design of a quarter of the unit cell with complex geometry.

when it is compressed. The average displacement in the Y-direction on the top boundary is $\bar{\mathbf{u}}_y = 30.02$, which is identical to the negative Poisson's ratio -0.75.

7.3.2 Unit cell with complex geometry

In the second example for material design, a unit cell with relatively complex geometry is optimized. It should be noted that as we focus on demonstrating the proposed method for complex topology, the manufacturability of the design isn't considered during the optimization. The target Poisson's ratio is $\nu = -0.5$. The corresponding target elastic properties are set as $C^{\star}_{1111} = 0.06$, $C^{\star}_{2222} = 0.06$ and $C^{\star}_{1122} = -0.03$, which are selected based on the results in [55]. The corresponding weights in the objective function are set as $\omega_{1111} = 0.5$, $\omega_{2222} = 0.5$ and $\omega_{1122} = 5$. The Young's modulus of the solid material is 1.0 and the Poisson's ratio is 0.2. The given volume fraction of the unit cell is 0.35. The unit cell is represented by quadratic B-splines boundaries. Quadratic Bézier triangles are used to discretize the design domain. The fine mesh is generated by uniformly refining the coarse mesh. At least four layers of elements are guaranteed within the thin connections.

The initial designs and the optimized designs of the quarter of the unit cell are shown in Fig. 32. Both coarse and fine meshes are plotted. The effective elastic tensor for the

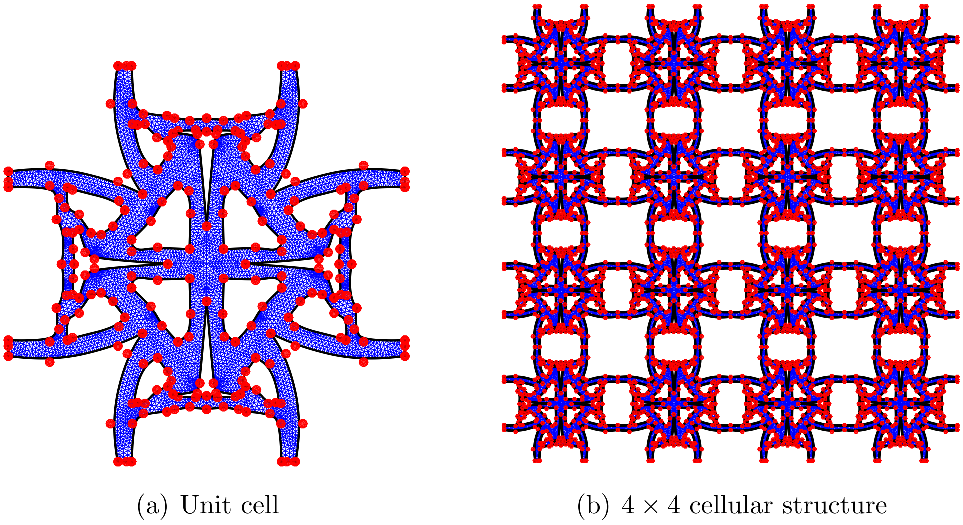
(a) Unit cell

(b) 4 × 4 cellular structure

Figure 33: Unit cell with complex topology and the periodically arranged cellular structure.

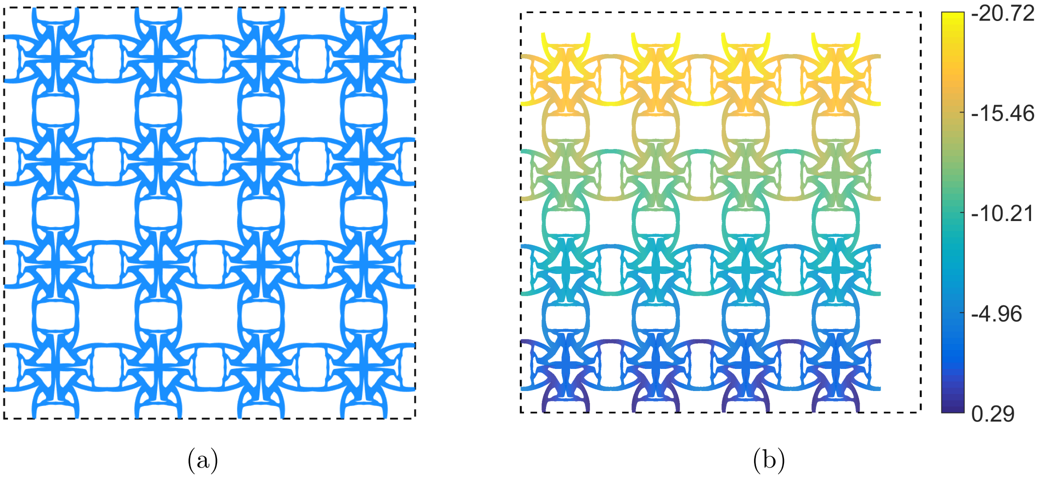

(a)

(b)

Figure 34: Numerical verification of the NPR behavior of the unit cell with complex geometry. (a) Initial shape. (b) Deformed shape.

optimized design is

$$C^H = \begin{bmatrix} 0.0599 & -0.03 & 0 \\ -0.03 & 0.0599 & 0 \\ 0 & 0 & 0.0022 \end{bmatrix}.$$

The corresponding Poisson's ratio is -0.5, which matches the desired value. The full unit cell and the periodically repeated 4 by 4 cellular structure are shown in Fig. 33. Numerical simulation is also conducted for this cellular structure to verify the NPR behavior. The boundary conditions of the simulation are same with those in Fig. 31(a). Figure 34 shows the initial and the deformed shapes. It can be observed that the structure shrinks laterally when axially compressed. The color contour in Fig. 31(b) shows the displacement in Y-direction. The average displacement at the top boundary is -20.323, which leads to the negative Poisson's ratio -0.508. This result matches very well with the designed NPR.

8 Conclusion

An isogeometric shape optimization method based on Bézier triangles is proposed in the work. For an input design model defined by B-spline boundary, the geometry is exactly parameterized by a coarse Bézier triangular mesh. For isogeometric analysis, a fine Bézier triangular mesh is used to represent physical fields. The coarse mesh is employed to maintain mesh quality and to solve a pseudo linear elasticity problem for mesh movement during the shape optimization. As the fine mesh retains the same geometric map as the coarse mesh, we can achieve high accuracy in analysis with the fine mesh and ensure mesh validity with the coarse mesh. This use of bi-level meshes is especially effective in shape optimization since the mesh Jacobian evaluation based on the coarse mesh will be computationally cheap.

For the selected benchmark problem, design of a plate with a hole, the proposed optimization method obtains the correct solution. The design of a cantilever with holes further demonstrates the ability of the proposed method to handle the design domains of complex topology. In the multi-hole cantilever design, as connections between holes in the final designs are overly thin and become single-element wide, a local refinement scheme is employed to generate multiple layers of elements within these thin connections to ensure analysis accuracy.

The proposed method is also employed to design materials with negative Poisson's ratio (NPR). The optimized unit cells are periodically repeated to generate cellular structures. These cellular structures are represented by B-splines boundary, which can be directly integrated into CAD systems for manufacturing. Bézier triangular mesh is also automatically generated for the cellular structures and the NPR behavior is verified through isogeometric analysis.

In order to ensure design boundary does not self-intersect, or become too close, a distance constraint is explicitly imposed. In order to efficiently check the distance between two B-spline curves, we cast the squared distance between Bézier curves into a Bézier form. The convex hull property of Bézier form is then used for quick check of the distance.

In our future work, the C^r-smooth Bézier triangles will be used to parameterize the design domain and represent the physical fields in order to take advantage of its computational efficacy [23, 24]. During the shape optimization process, as design boundary changes, how to construct valid C^r-smooth parameterization will be studied. Based on Bézier tetrahedra [25], the proposed method will also be extended to 3D problems.

9 Acknowledgement

The authors acknowledge the financial support from National Science Foundation grant #1435072 and #1404665 and ARO grant W911NF-17-1-0020.

References

[1] A Francavilla, CV Ramakrishnan, and OC Zienkiewicz. Optimization of shape to minimize stress concentration. *The Journal of Strain Analysis for Engineering Design*, 10(2):63–70, 1975.

[2] ME Botkin. Shape optimization of plate and shell structures. *AIAA Journal*, 20(2):268–273, 1982.

[3] Vincent Braibant and Claude Fleury. Shape optimal design using b-splines. *Computer Methods in Applied Mechanics and Engineering*, 44(3):247–267, 1984.

[4] Raphael T Haftka and Ramana V Grandhi. Structural shape optimizationa survey. *Computer Methods in Applied Mechanics and Engineering*, 57(1):91–106, 1986.

[5] Yeh-Liang Hsu. A review of structural shape optimization. *Computers in Industry*, 25(1):3–13, 1994.

[6] Grégoire Allaire, François Jouve, and Anca-Maria Toader. A level-set method for shape optimization. *Comptes Rendus Mathematique*, 334(12):1125–1130, 2002.

[7] J Norato, R Haber, D Tortorelli, and Martin P Bendsøe. A geometry projection method for shape optimization. *International Journal for Numerical Methods in Engineering*, 60(14):2289–2312, 2004.

[8] Thomas JR Hughes, John A Cottrell, and Yuri Bazilevs. Isogeometric analysis: Cad, finite elements, nurbs, exact geometry and mesh refinement. *Computer Methods in Applied Mechanics and Engineering*, 194(39):4135–4195, 2005.

[9] Wolfgang A Wall, Moritz A Frenzel, and Christian Cyron. Isogeometric structural shape optimization. *Computer Methods in Applied Mechanics and Engineering*, 197(33):2976–2988, 2008.

[10] Seonho Cho and Seung-Hyun Ha. Isogeometric shape design optimization: exact geometry and enhanced sensitivity. *Structural and Multidisciplinary Optimization*, 38(1):53–70, 2009.

[11] Xiaoping Qian. Full analytical sensitivities in nurbs based isogeometric shape optimization. *Computer Methods in Applied Mechanics and Engineering*, 199(29):2059–2071, 2010.

[12] Kang Li and Xiaoping Qian. Isogeometric analysis and shape optimization via boundary integral. *Computer-Aided Design*, 43(11):1427–1437, 2011.

[13] J Kiendl, R Schmidt, R Wüchner, and K-U Bletzinger. Isogeometric shape optimization of shells using semi-analytical sensitivity analysis and sensitivity weighting. *Computer Methods in Applied Mechanics and Engineering*, 274:148–167, 2014.

[14] Zhen-Pei Wang, Mostafa Abdalla, and Sergio Turteltaub. Normalization approaches for the descent search direction in isogeometric shape optimization. *Computer-Aided Design*, 82:68–78, 2017.

[15] Nguyen Dang Manh, Anton Evgrafov, Allan Roulund Gersborg, and Jens Gravesen. Isogeometric shape optimization of vibrating membranes. *Computer Methods in Applied Mechanics and Engineering*, 200(13):1343–1353, 2011.

[16] Xiaoping Qian and Ole Sigmund. Isogeometric shape optimization of photonic crystals via coons patches. *Computer Methods in Applied Mechanics and Engineering*, 200(25):2237–2255, 2011.

[17] Dang Manh Nguyen, Anton Evgrafov, and Jens Gravesen. Isogeometric shape optimization for electromagnetic scattering problems. *Progress in Electromagnetics Research B*, 45:117–146, 2012.

[18] Peter Nørtoft and Jens Gravesen. Isogeometric shape optimization in fluid mechanics. *Structural and Multidisciplinary Optimization*, 48(5):909–925, 2013.

[19] Attila P Nagy, Mostafa M Abdalla, and Zafer Gürdal. Isogeometric sizing and shape optimisation of beam structures. *Computer Methods in Applied Mechanics and Engineering*, 199(17):1216–1230, 2010.

[20] Attila P Nagy, Samuel T IJsselmuiden, and Mostafa M Abdalla. Isogeometric design of anisotropic shells: optimal form and material distribution. *Computer Methods in Applied Mechanics and Engineering*, 264:145–162, 2013.

[21] AH Taheri and Behrooz Hassani. Simultaneous isogeometrical shape and material design of functionally graded structures for optimal eigenfrequencies. *Computer Methods in Applied Mechanics and Engineering*, 277:46–80, 2014.

[22] Yu-Deok Seo, Hyun-Jung Kim, and Sung-Kie Youn. Isogeometric topology optimization using trimmed spline surfaces. *Computer Methods in Applied Mechanics and Engineering*, 199(49):3270–3296, 2010.

[23] Noah Jaxon and Xiaoping Qian. Isogeometric analysis on triangulations. *Computer-Aided Design*, 46:45–57, 2014.

[24] Songtao Xia, Xilu Wang, and Xiaoping Qian. Continuity and convergence in rational triangular bézier spline based isogeometric analysis. *Computer Methods in Applied Mechanics and Engineering*, 297:292–324, 2015.

[25] Songtao Xia and Xiaoping Qian. Isogeometric analysis with bézier tetrahedra. *Computer Methods in Applied Mechanics and Engineering*, 316:782–816, 2017.

[26] Krishna Kumar Saxena, Raj Das, and Emilio P Calius. Three decades of auxetics research- materials with negative poisson's ratio: A review. *Advanced Engineering Materials*, 18(11):1847–1870, 2016.

[27] Ole Sigmund. Materials with prescribed constitutive parameters: an inverse homogenization problem. *International Journal of Solids and Structures*, 31(17):2313–2329, 1994.

[28] Ole Sigmund. Tailoring materials with prescribed elastic properties. *Mechanics of Materials*, 20(4):351–368, 1995.

[29] Ulrik Darling Larsen, O Signund, and S Bouwsta. Design and fabrication of compliant micromechanisms and structures with negative poisson's ratio. *Journal of microelectromechanical systems*, 6(2):99–106, 1997.

[30] Anders Clausen, Fengwen Wang, Jakob S Jensen, Ole Sigmund, and Jennifer A Lewis. Topology optimized architectures with programmable poisson's ratio over large deformations. *Advanced Materials*, 27(37):5523–5527, 2015.

[31] Zhen-Pei Wang, Leong Hien Poh, Justin Dirrenberger, Yiling Zhu, and Samuel Forest. Isogeometric shape optimization of smoothed petal auxetic structures via computational periodic homogenization. *Computer Methods in Applied Mechanics and Engineering*, 2017.

[32] Carl De Boor, Carl De Boor, Etats-Unis Mathématicien, Carl De Boor, and Carl De Boor. *A practical guide to splines*, volume 27. Springer-Verlag New York, 1978.

[33] Gerald E Farin. *Curves and surfaces for CAGD: a practical guide.* Morgan Kaufmann, 2002.

[34] Xilu Wang and Xiaoping Qian. An optimization approach for constructing trivariate b-spline solids. *Computer-Aided Design*, 46:179–191, 2014.

[35] Hendrik Speleers and Carla Manni. Optimizing domain parameterization in isogeometric analysis based on powell–sabin splines. *Journal of Computational and Applied Mathematics*, 289:68–86, 2015.

[36] Songtao Xia, Guangyong Li, and Xiaoping Qian. Optimal shape for optical absorption in organic thin film solar cells. *Structural and Multidisciplinary Optimization*, 50(3):437–451, 2014.

[37] Chau Le, Tyler Bruns, and Daniel Tortorelli. A gradient-based, parameter-free approach to shape optimization. *Computer Methods in Applied Mechanics and Engineering*, 200(9):985–996, 2011.

[38] Kai-Uwe Bletzinger. A consistent frame for sensitivity filtering and the vertex assigned morphing of optimal shape. *Structural and Multidisciplinary Optimization*, 49(6):873–895, 2014.

[39] Xiaoping Qian. Topology optimization in b-spline space. *Computer Methods in Applied Mechanics and Engineering*, 265:15–35, 2013.

[40] AD Belegundu and SD Rajan. A shape optimization approach based on natural design variables and shape functions. *Computer Methods in Applied Mechanics and Engineering*, 66(1):87–106, 1988.

[41] Jens Gravesen, Anton Evgrafov, Dang-Manh Nguyen, and Peter Nørtoft. Planar parametrization in isogeometric analysis. In *International Conference on Mathematical Methods for Curves and Surfaces*, pages 189–212. Springer, 2012.

[42] Stanley Steinberg. *Fundamentals of grid generation.* CRC press, 1993.

[43] Lars V Ahlfors. Complex analysis: an introduction to the theory of analytic functions of one complex variable. *New York, London*, page 177, 1953.

[44] Myung-Jin Choi and Seonho Cho. A mesh regularization scheme to update internal control points for isogeometric shape design optimization. *Computer Methods in Applied Mechanics and Engineering*, 285:694–713, 2015.

[45] Xiao-Diao Chen, Linqiang Chen, Yigang Wang, Gang Xu, Jun-Hai Yong, and Jean-Claude Paul. Computing the minimum distance between two bézier curves. *Journal of Computational and Applied Mathematics*, 229(1):294–301, 2009.

[46] Xiao-Diao Chen, Weiyin Ma, Gang Xu, and Jean-Claude Paul. Computing the hausdorff distance between two b-spline curves. *Computer-Aided Design*, 42(12):1197–1206, 2010.

[47] Weihong Zhang, Gaoming Dai, Fengwen Wang, Shiping Sun, and Hicham Bassir. Using strain energy-based prediction of effective elastic properties in topology optimization of material microstructures. *Acta Mechanica Sinica*, 23(1):77–89, 2007.

[48] Behrooz Hassani and Ernest Hinton. A review of homogenization and topology optimization ihomogenization theory for media with periodic structure. *Computers & Structures*, 69(6):707–717, 1998.

[49] Behrooz Hassani and Ernest Hinton. A review of homogenization and topology optimization iiitopology optimization using optimality criteria. *Computers & structures*, 69(6):719–738, 1998.

[50] Panagiotis Vogiatzis, Shikui Chen, Xiao Wang, Tiantian Li, and Lifeng Wang. Topology optimization of multi-material negative poissons ratio metamaterials using a reconciled level set method. *Computer-Aided Design*, 83:15–32, 2017.

[51] Wenyu Chen, Rongdong Yu, Jianmin Zheng, Yiyu Cai, and Chikit Au. Triangular bézier sub-surfaces on a triangular bézier surface. *Journal of Computational and Applied Mathematics*, 235(17):5001 – 5016, 2011.

[52] Krister Svanberg. The method of moving asymptotesa new method for structural optimization. *International Journal for Numerical Methods in Engineering*, 24(2):359–373, 1987.

[53] Grégoire Allaire and Olivier Pantz. Structural optimization with freefem++. *Structural and Multidisciplinary Optimization*, 32(3):173–181, 2006.

[54] Fengwen Wang, Ole Sigmund, and Jakob Søndergaard Jensen. Design of materials with prescribed nonlinear properties. *Journal of the Mechanics and Physics of Solids*, 69:156–174, 2014.

[55] A Radman, X Huang, and YM Xie. Topological optimization for the design of microstructures of isotropic cellular materials. *Engineering optimization*, 45(11):1331–1348, 2013.

Appendix

The squared distance between two Bézier curves can also be represented as a Bézier form. Given two Bézier curves, $\mathbf{C}_1(u)$ and $\mathbf{C}_2(v)$, of degree m and n

$$\mathbf{C}_1(u) = \sum_{|\mathbf{i}|=m} \mathbf{P}_{\mathbf{i}} B_{\mathbf{i},m}(u), \quad u \in [0,1] \tag{56}$$

$$\mathbf{C}_2(v) = \sum_{|\mathbf{j}|=n} \mathbf{Q}_{\mathbf{j}} B_{\mathbf{j},n}(v), \quad v \in [0,1], \tag{57}$$

the squared distance function between these two curves reads

$$S(u,v) = \left(\sum_{|\mathbf{i}|=m} \mathbf{P}_{\mathbf{i}} B_{\mathbf{i},m}(u) - \sum_{|\mathbf{j}|=n} \mathbf{Q}_{\mathbf{j}} B_{\mathbf{j},n}(v) \right)^2 . \tag{58}$$

The Bézier form of $S(u,v)$ can be defined as

$$S(u,v) = \sum_{|\mathbf{r}|=2m} \sum_{|\mathbf{s}|=2n} D_{\mathbf{r},\mathbf{s}} B_{\mathbf{r},2m}(u) B_{\mathbf{s},2n}(v), \tag{59}$$

where $D_{\mathbf{r},\mathbf{s}} = A_{\mathbf{r}} + B_{\mathbf{s}} - 2E_{\mathbf{r},\mathbf{s}}$ are the squared distance ordinates and $A_{\mathbf{r}}$, $B_{\mathbf{s}}$ and $E_{\mathbf{r},\mathbf{s}}$ are denoted as

$$A_{\mathbf{r}} = \sum_{\substack{\mathbf{i}_1+\mathbf{i}_2=\mathbf{r} \\ |\mathbf{i}_1|=m \\ |\mathbf{i}_2|=m}} \frac{\binom{m}{\mathbf{i}_1}\binom{m}{\mathbf{i}_2}}{\binom{2m}{\mathbf{i}_1+\mathbf{i}_2}} (\mathbf{P}_{\mathbf{i}_1} \cdot \mathbf{P}_{\mathbf{i}_2}), \tag{60}$$

$$B_{\mathbf{s}} = \sum_{\substack{\mathbf{j}_1+\mathbf{j}_2=\mathbf{s} \\ |\mathbf{j}_1|=n \\ |\mathbf{j}_2|=n}} \frac{\binom{n}{\mathbf{j}_1}\binom{n}{\mathbf{j}_2}}{\binom{2n}{\mathbf{j}_1+\mathbf{j}_2}} (\mathbf{Q}_{\mathbf{j}_1} \cdot \mathbf{Q}_{\mathbf{j}_2}), \tag{61}$$

$$E_{\mathbf{r},\mathbf{s}} = \sum_{\substack{\mathbf{i}_1+\mathbf{i}_2=\mathbf{r} \\ |\mathbf{i}_1|=m \\ |\mathbf{i}_2|=m}} \frac{\binom{m}{\mathbf{i}_1}\binom{m}{\mathbf{i}_2}}{\binom{2m}{\mathbf{i}_1+\mathbf{i}_2}} \mathbf{P}_{\mathbf{i}_1} \cdot \sum_{\substack{\mathbf{j}_1+\mathbf{j}_2=\mathbf{s} \\ |\mathbf{j}_1|=n \\ |\mathbf{j}_2|=n}} \frac{\binom{n}{\mathbf{j}_1}\binom{n}{\mathbf{j}_2}}{\binom{2n}{\mathbf{j}_1+\mathbf{j}_2}} \mathbf{Q}_{\mathbf{j}_1}. \tag{62}$$

Figure 35(a) shows two cubic Bézier curves symmetric with respect to x-axis. The corresponding squared distance function and the ordinates are shown in Fig. 35(b). We can observe that the maximum ordinate is 8, which corresponds to the squared distance between $(0,1)$ and $(2,-1)$ or $(0,-1)$ and $(2,1)$, and the minimum distance happens at $u = 0.5$ and $v = 0.5$. We can also notice that for the two cubic curves, 49 distance ordinates are needed to represent the squared distance function.

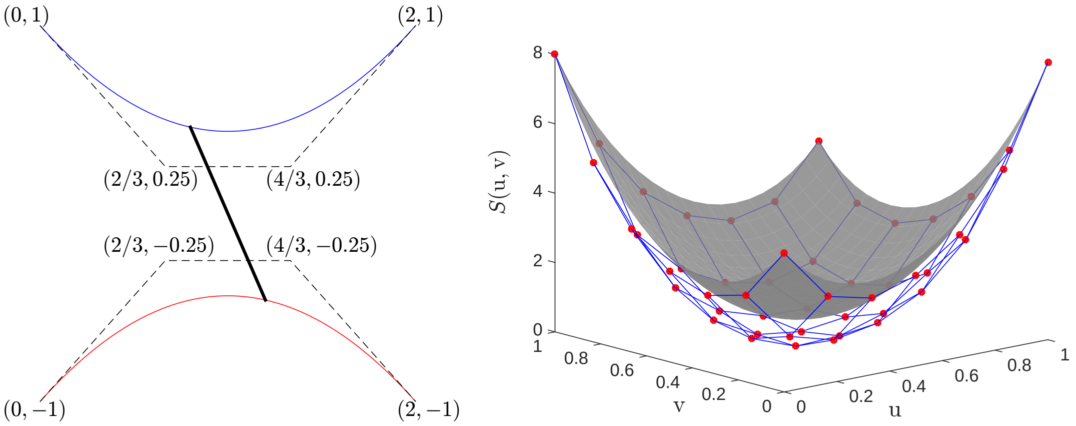

(a) Two Bézier curves

(b) The squared distance function

Figure 35: Squared distance between two Bézier curves.